Capacitive Micromachined Ultrasonic Transducers: Design, Fabrication and Characterization

by

Dilruba Zaman Jeba

A Thesis submitted to the Faculty of Graduate Studies of

The University of Manitoba

in partial fulfilment of the requirements of the degree of

Master of Science

Department of Electrical and Computer Engineering

University of Manitoba

Winnipeg

Abstract

Capacitive micromachined ultrasonic transducers (CMUTs) have been developed as an alternative to piezoelectric transducers for ultrasonic imaging in non-destructive testing applications. These CMUTs offer substantial advantages over their piezoelectric counterparts, which include a highly miniaturized system, easy integration with electronic control circuitry, a wider bandwidth, and a higher sensitivity. In this thesis, the design, fabrication and characterization of several single and array CMUT devices are reported. Many sizes of CMUTs, aiming to operate at different resonant frequencies, were fabricated using a PolyMUMPs sacrificial technique.

An analytical and finite element model was used to further understanding of the physical behaviour of the transducer. The basic functionality of the CMUT devices was investigated through capacitance and electrical impedance measurements. These devices showed greater change in the capacitance and impedance data while operating close to their collapse voltages. This higher change in both capacitance and impedance is a result of a larger membrane displacement. The acoustic output power is directly related to the magnitude of the membrane's displacement. The transducers performance thus can be enhanced by operating close to their collapse voltage and obtained higher sensitivity. The optical characterization, performed on the single devices and on the 1-D arrays, provided a better understanding of the membrane vibration modes and displacement profiles at different resonant frequency modes. Acoustic measurements were performed to demonstrate the transmission capability of the CMUTs. The generated acoustic signals were detected using a commercial detector. These acoustic experiments demonstrated that these CMUTs can potentially be used as ultrasonic transducers alternative to piezoelectric transducers.

Acknowledgements

Table of Contents

List of Figures

List of Tables

Chapter 1 Introduction

1.1 Research Motivation

Ultrasound is typically defined as a sound wave that has a frequency in the range from 20 kHz up to several gigahertz. Ultrasound technologies have historically been used for diagnosis and medical purposes. Several technologies are available for this purpose and some of these include magnetic resonance imaging (MRI), X-rays, and computerized tomography (CT) [1]. Among them, X-ray and CT imaging use ionizing radiation that can damage body tissue and hence requires limited exposure. In contrast, ultrasound is harmless and non-destructive compared to X-ray and CT imaging.

Ultrasound plays an important role in non-destructive evaluation (NDE), medical imaging, and acoustic microscopy. Ultrasound imaging is usually performed by sending a pulse and detecting the echo, which reflects back from the surface of an object. Depending on the flight time, as well as the strength and frequency component of the signal echo, the location, depth and physical nature of the object can be determined [2]. The ultrasound has a unique property to provide the information about an object, as sound can penetrate almost any material without causing harm. This property makes it a strong candidate for non-destructive imaging applications.

Polymeric insulated cables are widely used underground cables for high voltage applications around the world. The most commonly used insulating polymer material is cross-linked polyethylene (XPLE). Though XPLE cables are generally resistant to many chemicals and water, salts in the water eventually penetrate into the insulation. This phenomenon damages the underground cable and creates defects, which are

1

commonly known as the "water trees". With the formation of water trees, the cable structure is degraded permanently and reduces its breakdown strength. As such the service lifetime of underground XPLE cables is reduced [3]. Power interruption, due to failure of the XPLE insulation, is a major problem in the power industry. As a result of this cable damage, it is required to inspect the high voltage underground power cable in an effective, timely non-destructive manner.

Detection of water trees have been reported in the past [4]. The most common technique to detect water trees requires the dissection of the insulation to determine the electrical integrity [5]. The dissection method involves many steps and requires time to determine the level of damage. Detection of water tree location in XPLE insulation using ultrasound technology was demonstrated by Auckland et al. [6]. However, imaging of the water tree was challenging to perform due to the limitations of the computational capability of the data acquisition systems at that time [6], [7]. Recently, an improved image resolution has been achieved using a 2-D ultrasound synthetic aperture (SA) imaging technique that significantly reduced the data acquisition time [5].

The motivation for this project is to develop a non-destructive technique to detect and image water trees in the insulation of underground XPLE power cables. As the first step in the process, the design and fabrication of a new ultrasonic transducer was undertaken. Following the design and fabrication, the primary goal of this work is to characterize the ultrasonic transducers and have them operate as transducers.

1.2 Thesis Outline

This thesis is broken into seven chapters including this chapter. In Chapter 1, the motivation behind this project and the objective of this thesis work was briefly discussed.

The basic structure and working principle of a capacitive micromachined ultrasonic transducer (CMUT) is described in Chapter 2. The relevant background of ultrasonic transducers, and recent developments in the microelectromechanical systems (MEMS) ultrasonic transducers in particular are also presented.

In Chapter 3, analytical and finite element modeling of CMUT devices is presented. The modeling was performed to find some of the primary design parameters. The static, time dependant and acoustic behaviour of the CMUT devices was investigated using COMSOL electromechanical simulations. The effect of different design parameters, to maximize the transducer performance, was investigated and is discussed in this chapter.

The design parameters from the available fabrication facility are discussed in Chapter 4. Using those design parameters, some single devices and linear arrays were designed and fabricated. The fabrication process steps are also documented in this chapter.

The experimental results using the CMUT devices, obtained from the electrical and optical characterization, are presented in Chapter 5. As CMUTs are capacitive devices, the basic functionality of those devices was tested by measuring the change in the capacitance and the electrical impedance under various applied voltages. The

voltage limit for stable transducer operation was investigated for some of the devices. The effect of greater electrostatic force, produced by a greater DC bias voltage, on the membrane stiffness was also investigated and is described there. The vibration profile and the frequency spectrum of the single devices and arrays were measured using an optical measurement setup. The measurement setup and the results are also presented in Chapter 5.

In chapter 6, the acoustic characterization results of the fabricated CMUT devices are discussed. This discussion includes a demonstration of the transmitting capability of the CMUT device. The device was actuated using a burst/pulse signal with a DC bias applied on it. The generated ultrasonic signal, which was received by a commercial detector, is presented in this chapter.

Finally, a summary of this work and some suggestions for future work related to improving the current transducer designs are discussed in Chapter 7.

Chapter 2: Introduction to Capacitive Micromachined Ultrasonic Transducer (CMUT)

Ultrasonic transducers convert electrical energy into ultrasound and vice versa. They can be classified according to the mechanisms by which they convert the sound/electrical energy. Piezoelectric and electrostatic (i.e. capacitive) transducers are two of the most common type of ultrasonic transducers. Piezoelectric transducers are the most widely used ultrasonic transducers to generate and detect ultrasound. The piezoelectric transducers generate sound waves by compressing and expanding the piezoelectric crystals in response to an electric signal, as shown in Figure 2.1 (a).

On the other hand, capacitive transducers are comprised of a flexible membrane separated from a rigid plate by air (see Figure 2.1 (b)). They generate ultrasonic waves by varying the applied electric field across the gap which subsequently induces a mechanical force causing the membrane to move. Both piezoelectric and capacitive transducers have successfully been used for generating and sensing ultrasonic waves [8], [9]. However, the usefulness of piezoelectric transducers has been compromised by the complex fabrication required and a large acoustic mismatch between the piezoelectric crystals and the surrounding medium (i.e. air). The fabrication process of piezoceramic material lead zirconate titanate (PZT) requires a number of steps and manual labour which starts with a PZT material bonded with a backing material, electrodes, and matching layers and then manually diced in to elements. Reducing the element size or further increasing the number of elements has impact on the fabrication

process. In comparison, capacitive transducers have shown better impedance matching with the medium than the piezoelectric transducers [10].

Expansion   Compression

(a)

Ultrasound

No electric field   Membrane moving with applied electric field

(b)
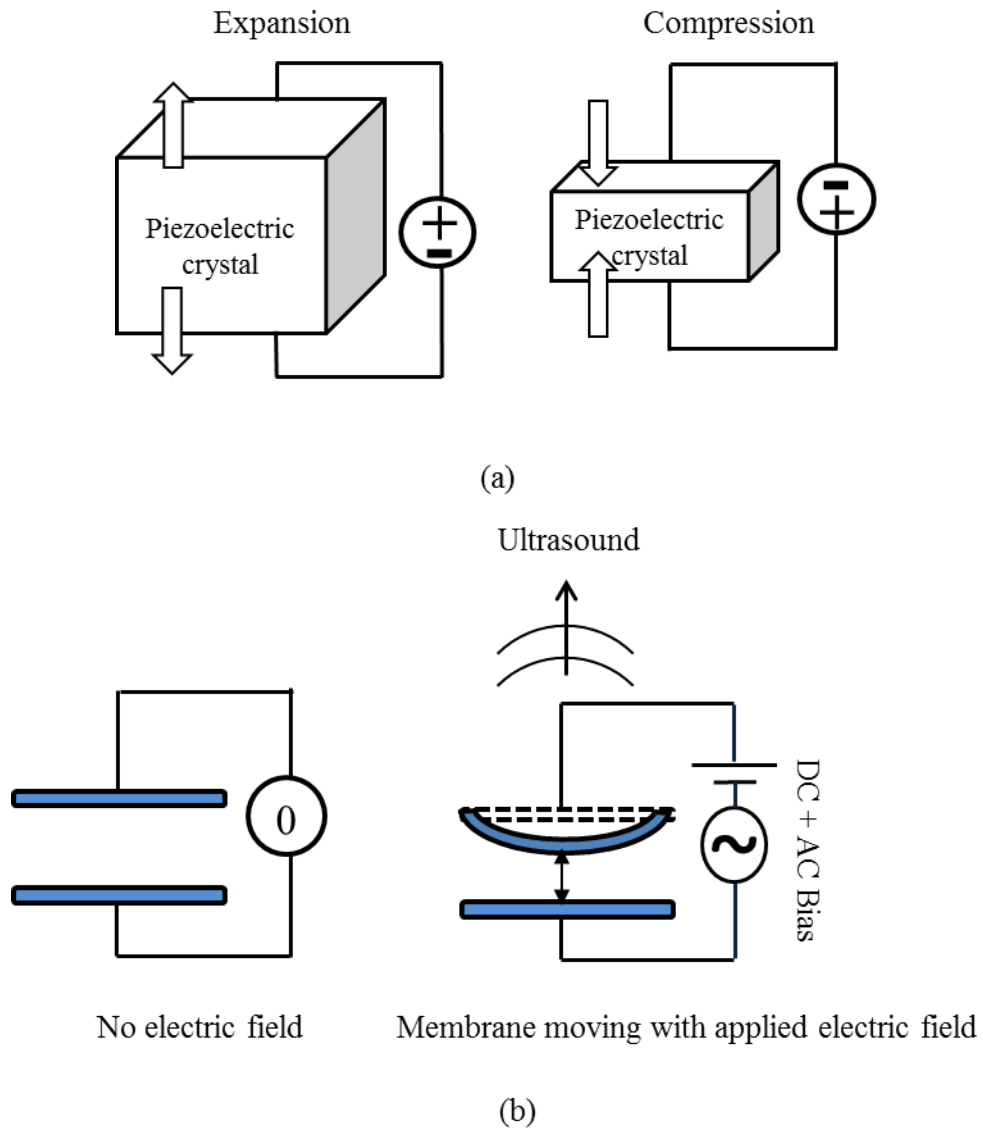
Figure 2.1. Operation of a (a) piezoelectric transducer (b) capacitive transducer.

The capacitive transducer was first demonstrated in air in 1954 [9] and in immersion in 1979 [11]. Generally, capacitive transducers require a high electric field strength to enable significant membrane vibration and to generate ultrasonic waves. As a result, mechanical breakdown of the transducer may occur due to the high electric

6

field. This mechanical breakdown can be avoided by optimal device design, which requires the careful selection of membrane material, membrane thickness, and the gap height [12].

Recent developments in microelectromechanical systems technology (MEMS) have facilitated the fabrication of small transducer structures with dimensions on the order of nanometers to micrometers. This MEMS fabrication technology has permitted the introduction of a different type of capacitive ultrasonic transducer: the capacitive micromachined ultrasonic transducer (CMUT). The capacitive micromachined ultrasonic transducer (CMUTs) were first introduced in 1993 by M. Haller and B.T. Khuri-Yakub [13]. The imaging results from the CMUTs showed wider bandwidth and better sensitivity relative to standard piezoelectric devices [14]. Researchers have also produced a variety of real time imaging techniques using CMUTs for non-destructive testing and for medical imaging [15], [16] .

2.1 Principle Operation of a CMUT:

The cross sectional schematic view of a capacitive micromachined ultrasonic transducer (CMUT) is shown in Figure 2.2. A basic CMUT consists of a thin membrane which is suspended over a substrate and separated by a cavity. Typically, the membrane is metalized and acts as the top electrode of the "capacitor". A highly doped silicon substrate or another conductive plate can act as the bottom electrode. The outer edge of the membrane is rigid and typically fixed to the substrate by a post which may be conductive or insulating, depending upon the details of the design. An insulating layer may be deposited on the bottom electrode to avoid shorting the membrane and the substrate at high voltages (see Figure 2.2).
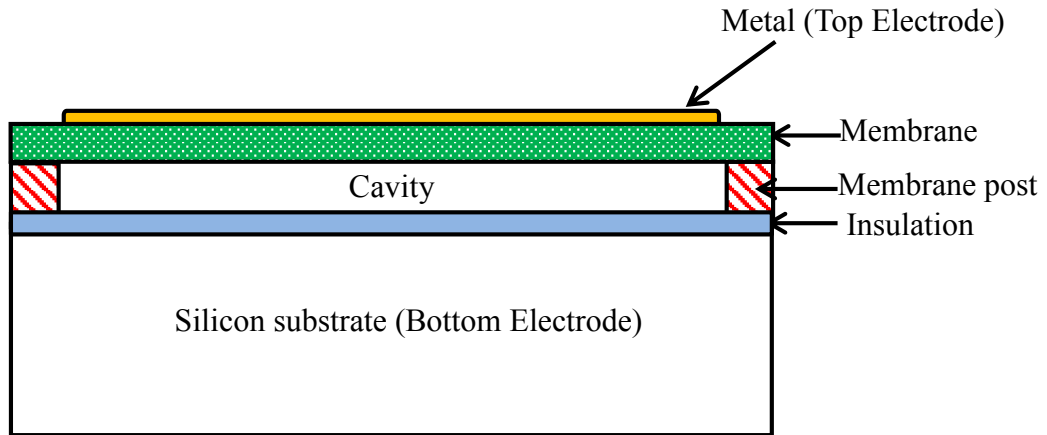
Figure 2.2. Schematic view of a capacitive micromachined ultrasonic transducer (CMUT).

The principle operation of a CMUT is based on the production of an electrostatic force between top and bottom electrodes through an applied bias. When a DC bias is applied between the top metalized membrane and the bottom silicon substrate, the induced electrostatic force pulls the top membrane toward the bottom electrode. The electrostatic force is balanced by the membrane restoring spring force, which arises from the membrane stiffness. Superimposing ac voltage signal on the DC bias actuates the membrane causing it to vibrate and generates acoustic waves into the surrounding medium. This is referred to as the transmitting mode of the transducer and is shown in Figure 2.3 (a).

(a)

(b)
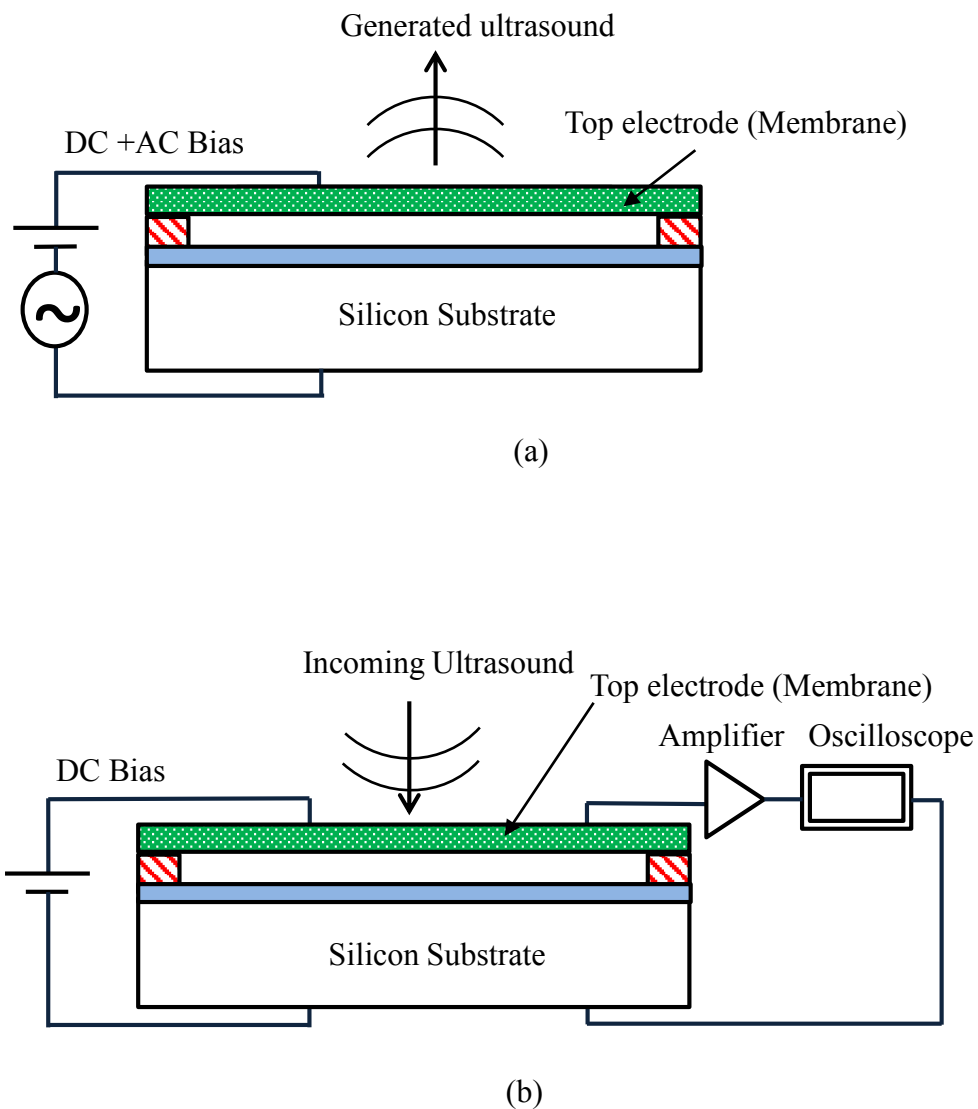
Figure 2.3. CMUT as (a) a transmitter (b) a receiver.

In receiving mode, the CMUT is biased with a DC voltage to attract the membrane closer to the bottom electrode which causes an initial bending of the membrane. When this CMUT is subjected to an acoustic wave, the membrane experiences mechanical vibration, causing a change in the device capacitance, and generating an alternating current. The amplitude of the current can be measured using a high impedance amplifier as shown in Figure 2.3 (b).

A CMUT is typically fabricated in large 1-D or 2-D arrays with hundreds of CMUT cells using a MEMS fabrication technique, where the cells are connected together. A large array of cells, when actuated at the same time, can produce a larger output signal, and a more sensitive output response than a single device.

2.2 Advantages and Challenges of CMUTs:

Piezoelectric transducers have historically been the commercial standard for detecting and imaging of objects for many different applications. Piezoelectric transducers, typically made of quartz or lead zirconate, however have some drawbacks [12]. The drawbacks include a complex fabrication process, a narrow bandwidth, and a poor impedance matching in air or in immersion medium. The typical acoustic impedance of a piezoelectric material ($\sim 30 \times 10^6$ Kg/m^2.s) is several orders larger in magnitude than air (~ 400 kg/m^2·s) and about a factor of 20 or so for water ($\sim 1.48 \times 10^6$ kg/m^2·s) [17]. This large impedance mismatch makes the piezoelectric transducers challenging to be used in air, and requires an extra matching layer to couple the ultrasound into air medium. Moreover, piezoelectric materials generally produce a large acoustic power at or near their resonant frequency and hence provide narrow bandwidth [18]. Also integration with silicon based control circuits is not easy, as piezoelectric transducers and silicon based circuits are fabricated using different fabrication techniques.

Capacitive micromachined ultrasonic transducers have overcome some of the piezoelectric transducer's drawbacks and offer some other advantages, such as batch fabrication of large density arrays to any shape and size, a broader bandwidth and a better impedance matching [10], [12], [18]. The most commonly used membrane

materials for MEMS ultrasonic transducer include silicon nitride, polysilicon and silicon [19], [20], [21]. The density and acoustic velocity of those materials permit a significant impedance matching with the surrounding medium. Furthermore, micromachining fabrication (MEMS) technology makes it possible to fabricate microstructures in high quality, uniform arrays. This technology also gives flexibility to fabricate the transducers in a variety of shapes and sizes, which allows designers to fabricate devices that can operate over a wider frequency range.

Capacitive transducers have not historically shown high performance and the penetration of the generated ultrasound into a material was not satisfactory as compared to piezoelectric transducers [15]. Dielectric charging is another drawback of CMUTs while using dielectric materials (e.g. silicon nitride) either as the membrane or as the substrate insulating layer. Charge that may be induced during the fabrication process or that may arise due to the strong applied electric field may become "trapped". This trapped charge will induce an electric field which could prevent the membrane from returning back to its resting position and eventually degrade the reliability and performance [22].

2.3 Recent Developments in MEMS transducers:

Many developments in the CMUT have been reported since its invention [15], [23], [24]. Recently, Hitachi Medical Corporation have produced a commercial CMUT probe for medical ultrasound [25]. Several micromachining fabrication technologies (i.e., surface micromachining, bulk micromachining) have been used to fabricate MEMS ultrasonic transducers. In the surface micromachining technique, structures are fabricated in thin films deposited on the substrate and the desired structure is created

11

by releasing the sacrificial layer. Bulk micromachining, which is different from the surface micromachining, allows etching through the back side of the wafer to form the desired structure. Capacitive ultrasonic transducers have been successfully fabricated using surface micromachining techniques [26], [27], [28], [29], [30]. Bulk micromachining process (e.g. Silicon on Insulator (SOI) wafer bonding) was first reported by Huang et al. [31]. Using a surface micromachining techniques, a membrane is deposited over a sacrificial layer which is later removed through etch holes in the membrane. After removing the sacrificial layer, the membrane etch holes need to be sealed to create vacuum gap and these steps are considered as limitations in the surface micromachining process. A large membrane also can not be created because of the stress issues of thin films. In contrast, the wafer bonding process solves this limitation by forming a vacuum cavity gap by bonding two wafers and allows fabrication of CMUTs with large membranes. The bulk micromachining process is therefore more preferable fabrication technique than surface micromachining [32].

Finite element modeling was developed to further understand the CMUT operating characteristics [33]. Researchers have also fabricated and characterized 1-D and 2-D arrays [34], [35]. Ultrasound imaging using CMUTs has been demonstrated and reported by several research groups [23], [36], [37]. A 3-D photo acoustic image was also reported using 2-D CMUT arrays [38].

Chapter 3 Modeling of CMUTs

3.1 Analytical modeling of CMUTs

The dynamics of a capacitive micromachined ultrasonic transducer (CMUT) is similar to a parallel plate capacitor. To understand the fundamentals of a CMUT device, an analytical model was used based on a plate vibration theory. Some of the basic characteristic parameters were found from this analytical model which was used as the primary design strategy. Analytical modeling of capacitive micromachined ultrasonic transducers (CMUTs), based on a plate vibration theory, has been reported by several researchers [39]. The analytical model used for the design and optimization of the CMUTs is described in this chapter.

3.2 Mass-Spring-Capacitor System

A schematic diagram of a capacitive micromachined ultrasonic transducer (CMUT), shown in Figure 2.2, can be viewed as a parallel plate capacitor where the top plate is moveable, and separated from the fixed bottom plate by an air gap. If the gap between two plates is small compared to the lateral dimension of the plates, the plates can be considered as the parallel plates [39]. When the top plate moves, the stiffness of the plate introduces a restoring spring force which opposes the electrostatic force. Therefore, a CMUT can be represented as an electro-mechanical system with one degree of freedom [39]. This electro-mechanical system consists of a spring k, a mass m and a parallel plate capacitor C, shown in Figure 3.1. To simplify the electro-mechanical analysis, the following approximations were made:

1. The deflection of the top plate is very small compared to the air gap and the restoring spring force is a function of the displacement.

2. The displacement of the plate is considered to be uniform all over the surface.

3. Electrical fringing field is neglected as the plate is clamped at the edge.

4. The plate is vibrating in vacuum and therefore no loading effect is considered.

5. Residual stress of the plate is neglected.

The total force acting on the plate under an applied bias can be written as:

$$F_{Mass} = F_{Spring} + F_{Electrostatic} \text{,}$$ 3.1

where F_{Mass} represents the force due to the mass, F_{Spring} is the restoring spring force exerted by the elasticity of the plate and $F_{Electrostatic}$ is the electrostatic force between two parallel plates induced by the applied voltage.
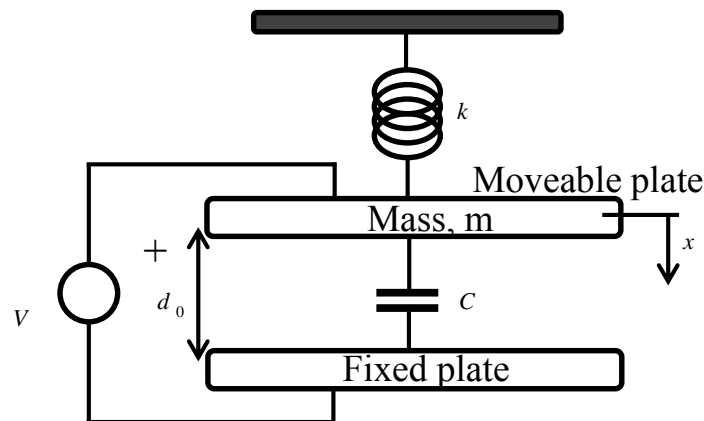
Figure 3.1. A mass-spring electromechanical model with a parallel plate capacitor.

The electrostatic force, generated by an applied DC bias, between two parallel plates, can be written as [39]

$$F_{Electrostatic} = -\frac{d}{dx}\left(\frac{1}{2}CV^2\right) = -\frac{1}{2}V^2\frac{d}{dx}\left(\frac{\varepsilon A}{d_0 - x}\right) = \frac{\varepsilon AV^2}{2(d_0 - x)^2},$$ 3.2

where ε is the dielectric permittivity of the material between two plates, A is the plate area, V is the applied bias, d_0 is the initial gap height, and x is the initial plate displacement under a static bias. The dielectric permittivity, ε can be written as $\varepsilon = \varepsilon_r \varepsilon_0$, where ε_r is the relative permittivity of the dielectric material, for air $\varepsilon_r \sim 1$ and ε_0 is the dielectric permittivity of space, and therefore $\varepsilon = \varepsilon_0$.

When a voltage is applied, the electrostatic force pulls the top plate toward the bottom plate, and causes the reduction of gap height. The capacitance between two plates may be expressed as:

$$C = \frac{\varepsilon A}{d_0 - x}$$ 3.3

The mechanical spring also produces a restoring force that is proportional to the displacement of the plate and can be written using Hooke's law,

$$F_{Spring} = -kx,$$ 3.4

where k is the stiffness of the plate.

For an applied voltage, $V(t) = V_{DC} + V_{AC}\sin(\omega t)$, substituting all the force expressions into Equation 3.1, a time dependant behaviour of the system can be found to be

$$m\frac{d^2x}{dt^2} - \frac{\varepsilon AV(t)^2}{2(d_0 - x)^2} + kx = 0,$$ 3.5

where V_{DC} is the DC voltage, V_{AC} is ac voltage, ω is the operating frequency and m is the mass of the plate.

Therefore, a CMUT can be modeled as a mass-spring-capacitor electromechanical system, where the CMUT membrane is the moveable plate and the substrate is the fixed bottom plate. Using this model, the theoretical operation of CMUTs is derived in the following sections including some design parameters, such as: collapse voltage, resonant frequency, and radiated pressure.

3.3 Collapse Voltage

For static operation, only DC bias is considered to be applied to the CMUT membrane. At equilibrium, the electrostatic force is balanced by the spring force and hence the condition for force balance becomes [39]

$$F_{Electrosta\ tic} = -F_{Spring} \qquad \text{3.6}$$

$$\frac{\varepsilon A V_{DC}^{\ 2}}{2(d_0 - x)^2} = kx \qquad \text{3.7}$$

Both $F_{Electrosta\ tic}$ and $\left| F_{Spring} \right|$ are the functions of displacement (see Equations 3.2 and 3.4). The intersection of these two functions, shown in Figure 3.2, gives two points: a and b [40]. At point a and b, the electrostatic force is equal to the spring force, hence net force on the membrane is zero. Though the membrane is at equilibrium at point a and b, point b is not a stable state. Just after crossing point b, the electrostatic force overcomes the membrane spring force and a small disturbance will cause the membrane to deflect forward continuously until collapsing on the bottom electrode.

16

Hence, to maintain a stable operation, the rate of increasing electrostatic force (slope of $F_{Electrosta\ tic}$) should be less than the rate of increasing spring force (slope of $\left|F_{Spring}\right|$) so that the membrane is pushed back to its equilibrium position.
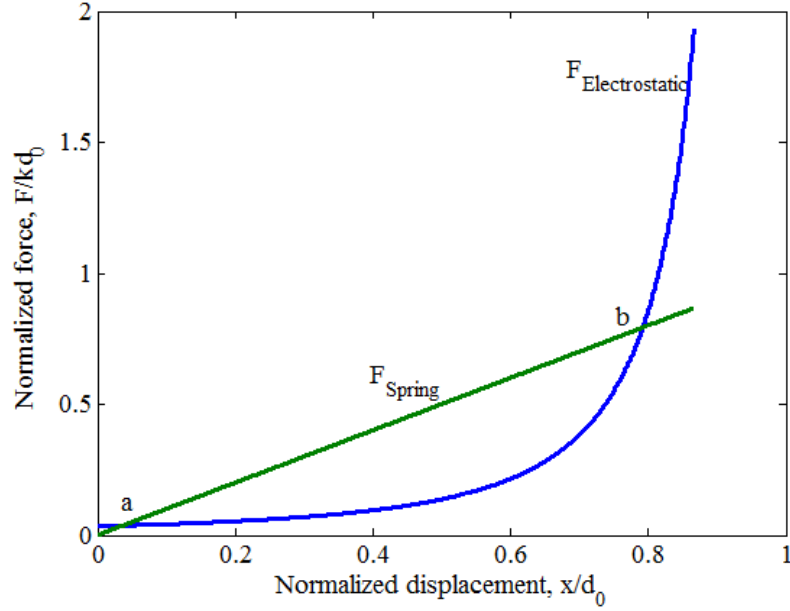
Figure 3.2. The dependency of electrostatic force and opposing spring force as a function of displacement, for a given dimension of device with a given membrane thickness and gap height.

The condition for the stable state can be mathematically written as [40]

$$\frac{d(F_{Electrostatic} + F_{Spring})}{dx} < 0 \qquad\qquad 3.8$$

Combining Equation 3.8 with 3.6 yields:

$$\frac{\epsilon A V_{DC}{}^2}{(d_0 - x)^3} - k < 0 \qquad\qquad 3.9$$

$$\frac{\epsilon A V_{DC}{}^2}{(d_0 - x)^3} < k \qqquad\qquad 3.10$$

Simplifying with Equation 3.7

$$\frac{\epsilon A V_{DC}{}^2}{(d_0 - x)^3} < \frac{\epsilon A V_{DC}{}^2}{2x(d_0 - x)^2} \qquad\qquad 3.11$$

$$\frac{1}{(d_0 - x)} < \frac{1}{2x} \qquad\qquad 3.12$$

$$x < \frac{d_0}{3} \qquad\qquad 3.13$$

This means that the operation is stable as long as the displacement is less than one third of the original gap height. However the electrostatic force increases quadratically with the applied voltage. When the displacement of the membrane becomes higher than one third of the original gap height ($\frac{d_0}{3}$), the electrostatic force overcomes the spring force. The membrane displacement greater than $\frac{d_0}{3}$ causes a mechanical breakdown of the device by collapsing the membrane onto the substrate. The voltage at which this phenomenon occurs, is referred to as the "collapse voltage".

The collapse voltage can be found by considering the previously mentioned stable point (Equation 3.13) and rearranging Equation 3.7 yields [40]

$$V_{collapse} = \sqrt{\frac{8\,k\,d_0{}^3}{27\,\varepsilon\,A}}\,, \qquad\qquad 3.14$$

where $A = \pi R^2$ is the membrane area, R is the membrane radius and k is the spring constant.
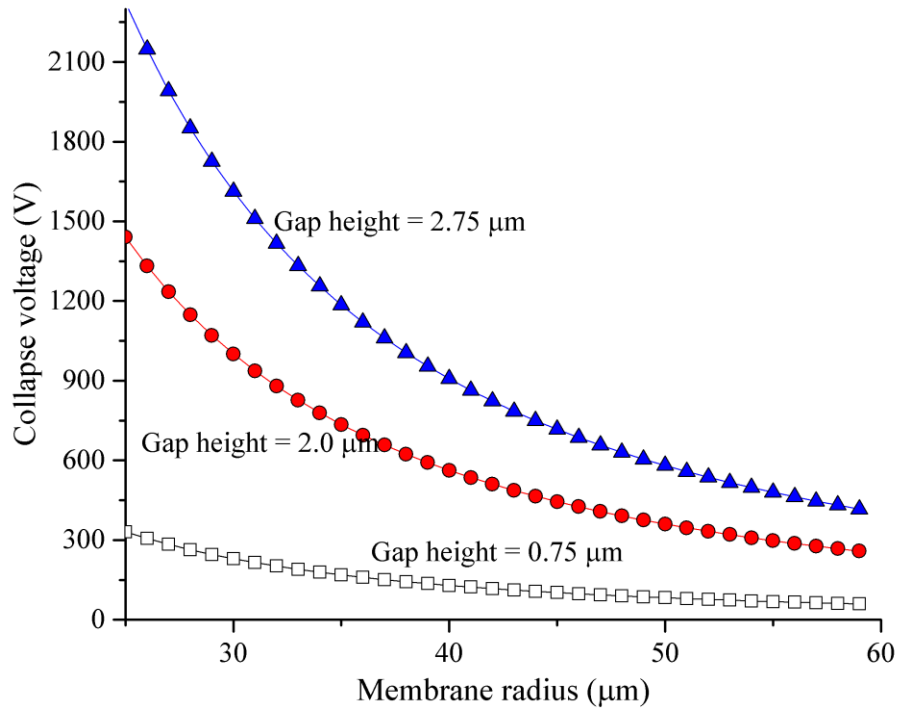
Figure 3.3. Analytical collapse voltage as a function of membrane radius and gap height at a given membrane thickness.

The graphical presentation of Equation 3.14 is shown in Figure 3.3. It can be seen from the figure that lower gap heights and larger radii offer lower collapse voltages, and subsequently a lower power consumption. Therefore, in order to minimize driving voltage and increase sensitivity, a CMUT's voltage operating range can be modified by optimizing the gap height and the membrane dimension for a given membrane thickness.

From the schematic diagram of a basic CMUT, shown in Figure 2.2, it can be seen that an insulating layer was deposited on the bottom electrode to avoid shorting the membrane to the substrate at high voltages. Therefore, the insulating layer, which is in series with the air gap, needs to be included in the expression of air gap height. By

calculating the series capacitance between the air and the insulating layer, the expression for the gap height can be written as:

$$C_{air+insulation} = \frac{C_0 \times C_i}{C_0 + C_i} \qquad 3.15$$

$$= \frac{\varepsilon_0 \times \varepsilon_i \times A}{\varepsilon_0 d_i + \varepsilon_i d_0} \qquad 3.16$$

$$= \frac{A}{\dfrac{d_o}{\varepsilon_0} + \dfrac{d_i}{\varepsilon_i}} \qquad 3.17$$

$$d = \frac{d_o}{\varepsilon_0} + \frac{d_i}{\varepsilon_i}, \qquad 3.18$$

where C_0 and C_i are the capacitance of the dielectric material (i.e. air) and the insulating layer respectively, d_o is the initial gap height, d_i is the insulator thickness, ε_0 and ε_i are the relative dielectric permittivity of air ($\varepsilon_0 = 1$) and insulating material respectively, and d is the gap height.

As the membrane deflects under an applied bias, the gap height decreases as the membrane is displaced (x) toward the bottom electrode. The effective gap height may be written as [10]

$$d_{eff} = d_o + \frac{d_i}{\varepsilon_i} - x \qquad 3.19$$

As collapse voltage is a function of gap height, the expression for the collapse voltage (Equation 3.14) can be modified using the effective gap height (Equation 3.19) [10] to yield

$$V_{collapse} = \sqrt{\frac{8 \, k \, d_{eff}{}^3}{27 \, \varepsilon \, A}}$$ 3.20

The effective gap height, d_{eff} increases with an additional insulating layer in series. This additional layer makes the collapse voltage even higher than that of without an additional insulating layer. As the collapse occurs when the membrane deflection is one third of the effective gap height, due to this additional layer the voltage requirement for the membrane to collapse effectively increases. Therefore, the thickness of the insulating layer is another design parameter that can be used to mitigate the mechanical breakdown of CMUT devices [41].

3.4 Dynamic Operation

For dynamic operation, an ac voltage signal is applied with the DC bias between the two electrodes. The ac voltage magnitude is typically much smaller than the DC bias which causes a small perturbation to the membrane. This perturbation of the membrane produces an ultrasound pressure wave. For an applied bias $V(t) = V_{DC} + V_{AC} \sin(\omega t)$, the force acting on the membrane is given by

$$F_{DC+AC} = \frac{\varepsilon A V(t)^2}{2(d_0 - x)^2}$$ 3.21

$$= \frac{\varepsilon A (V_{DC} + V_{AC} \sin \omega t)^2}{2(d_0 - x)^2}$$ 3.22

$$= \frac{\varepsilon A}{2(d_0 - x)^2}\left[(V_{DC}{}^2 + \frac{1}{2}V_{AC}{}^2) + 2V_{DC}V_{AC} \sin \omega t - \frac{1}{2}V_{AC}{}^2 \cos(2\omega t) \right]$$ 3.23

$$= \frac{\varepsilon A}{2(d_0 - x)^2}\left(F_0 + F_1 + F_2 \right)$$ 3.24

If the driving frequency ω is close to the resonant frequency, the effect of $F_1 (= 2V_{DC} V_{AC} \sin \omega t)$ will be much larger due to the mechanical resonance than that of $F_2 (= \frac{1}{2} V_{AC}^2 \cos(2\omega t))$. The effect of F_2 is hence considered to be very small and can be neglected. The force expression can be simplified as

$$F_{DC+AC} \approx \frac{\varepsilon A}{2(d_0 - x)^2} \left(V_{DC}^2 + \frac{1}{2} V_{AC}^2 + 2V_{DC} V_{AC} \sin \omega t \right) \qquad 3.25$$

$$\approx \frac{\varepsilon A}{2(d_0 - x)^2} \left(V_{DC}^2 + 2V_{DC} V_{AC} \right) \text{, if } V_{DC} >> V_{AC} \qquad 3.26$$

$$\approx \frac{\varepsilon A}{2(d_0 - x)^2} V_{DC}^2 + \frac{\varepsilon A V_{DC}}{(d_0 - x)^2} V_{AC} \qquad 3.27$$

The first part of the force expression in Equation 3.27 pulls the top electrode closer to the bottom electrode which effectively increases the transducer's sensitivity. The applied ac voltage signal causes the membrane to vibrate and produces an ultrasonic wave, as shown in the second term of Equation 3.27. For the transmission operation, a DC bias is essential with an ac voltage so that the electrodes already get closer and the ac voltage exerts a larger force to generate ultrasound. In the receiving operation, a DC bias is required to have charge on the membrane to detect any kind of change in the capacitance in the form of an alternating current due to an incoming pressure wave.

3.5 Spring Softening Coefficient and Resonant Frequency

As V_{DC} is increased, the electrostatic force increases quadratically and pulls the membrane closer to the substrate. As the membrane gets closer to the bottom electrode,

the generated electrostatic force modifies the spring constant of the membrane. This effect can be interpreted as the spring softening effect [42] and can be realized by the mathematical expansion of Equation 3.2 into a Taylor series at a minimum displacement point $x = x_0$ [39], [43]:

The Taylor series expansion of a function $f(x)$ at a point $x = x_0$ is given by

$$f(x) = f(x_0) + f^{/}(x_0)(x - x_0) + \frac{f^{//}(x_0)}{2!}(x - x_0)^2 + \cdots$$

3.28

$$F_{Electrostatic} = \frac{\epsilon A V^2}{2}\frac{1}{(d_0 - x)^2}$$

3.29

Taking the Taylor series expansion of $F_{Electrostatic}$ gives

$$= \frac{\epsilon A V^2}{2}\left[\frac{1}{(d_0 - x)^2}|_{x=x_0} + \frac{(-2)(-1)}{(d_0 - x)^3}|_{x=x_0}(x - x_0) + \cdots..\right]$$

3.30

$$= \frac{\epsilon A V^2}{2(d_0 - x_0)^2}\left[1 + 2\frac{x - x_0}{d_0 - x} + ..\right]$$

3.31

Substituting $F_{Electrostatic}$ into Equation 3.5

$$m\frac{d^2x}{dt^2} - \frac{\epsilon A V^2}{2(d_0 - x_0)^2}\left[1 + 2\frac{x - x_0}{d_0 - x_0} + ..\right] + kx = 0$$

3.32

$$m\frac{d^2x}{dt^2} - \frac{\epsilon A V^2}{2(d_0 - x_0)^2} - \frac{\epsilon A V^2}{(d_0 - x_0)^3}x + \frac{\epsilon A V^2}{2(d_0 - x_0)^2}x_0 + .. + kx = 0$$

3.33

After rearranging Equation 3.33,

$$m\frac{d^2x}{dt^2} + \left(k - \frac{\epsilon A V^2}{(d_0 - x_0)^3}\right)x - \left(\frac{\epsilon A V^2}{2(d_0 - x_0)^2} - \frac{\epsilon A V^2 x_0}{(d_0 - x_0)^3}\right) = 0$$

3.34

$$m\frac{d^2x}{dt^2} + \left(k - k_{soft}\right)x - \left(\frac{\epsilon A V^2}{2(d_0 - x_0)^2} - \frac{\epsilon A V^2 x_0}{(d_0 - x_0)^3}\right) = 0,$$

3.35

where

$$k_{soft} = \frac{\epsilon A V^2}{(d_0 - x_0)^3} \qquad 3.36$$

At resting position, $x_0 = 0$, the terms can be rearranged as follows

$$m\frac{d^2x}{dt^2} + \left(k - \frac{\epsilon A V^2}{d_0^3}\right)x - \frac{\epsilon A V^2}{2d_0^2} = 0, \qquad 3.37$$

where k_{soft} is the spring softening coefficient.

It can be noted from Equation 3.35 that the electrostatic force due to an applied bias changes the spring constant of the system. The overall spring constant is decreased by a factor k_{soft} with an increased DC bias, which means the membrane becomes less stiff. As the voltage is increased, the ratio $\left|\frac{k_{soft}}{k}\right|$ increases significantly which affects the elasticity of the membrane significantly. This modification in spring constant due to an increased electrostatic force is termed as the "spring softening effect".

The deflection of a clamped membrane at the resting position at radial distance, r is given by [44]

$$x = \frac{3(1 - v^2)P}{16\,Eh^3}(R^2 - r^2)^2, \qquad 3.38$$

where P is uniformly distributed pressure due to an applied bias, v is the Poisson's ratio of the membrane material, E is the Young's modulus of the membrane material, R is the membrane radius, h is the membrane thickness, and r is the radial distance. For a membrane clamped at the edge, the maximum displacement which occurs at the center of the membrane, ($r = 0$) is calculated as

$$x_{max} = \frac{3(1-v^2)P}{16\,Eh^3}R^4 \qquad\qquad 3.39$$

$$= \frac{3(1-v^2)}{16\,Eh^3} \times \frac{-F_{spring}}{\pi R^2} \times R^4 \qquad\qquad 3.40$$

Rearranging, the spring force may now be given by

$$x_{max} \times \frac{16\,\pi Eh^3}{3(1-v^2)R^2} = -F_{spring}\quad, \qquad\qquad 3.41$$

where P is uniformly distributed pressure due to an applied bias, F_{spring} is the spring

force which is equal and opposite in direction of P, x_{max} is the membrane center

deflection.

Comparing Equation 3.4 and 3.41,

$$k = \frac{16\,\pi Eh^3}{3(1-v^2)R^2} \qquad\qquad 3.42$$

The reduced spring constant, $k - k_{soft} = \dfrac{16\,\pi Eh^3}{3(1-v^2)R^2} - \dfrac{\varepsilon A V_{DC}^2}{d_0^3}$ \qquad 3.43

    Equation 3.43 reveals a nonlinear behaviour of the spring constant of a

membrane. The spring stiffness of the membrane obviously decreases with increasing

voltage (shown in Figure 3.4), which causes the membrane to vibrate more.
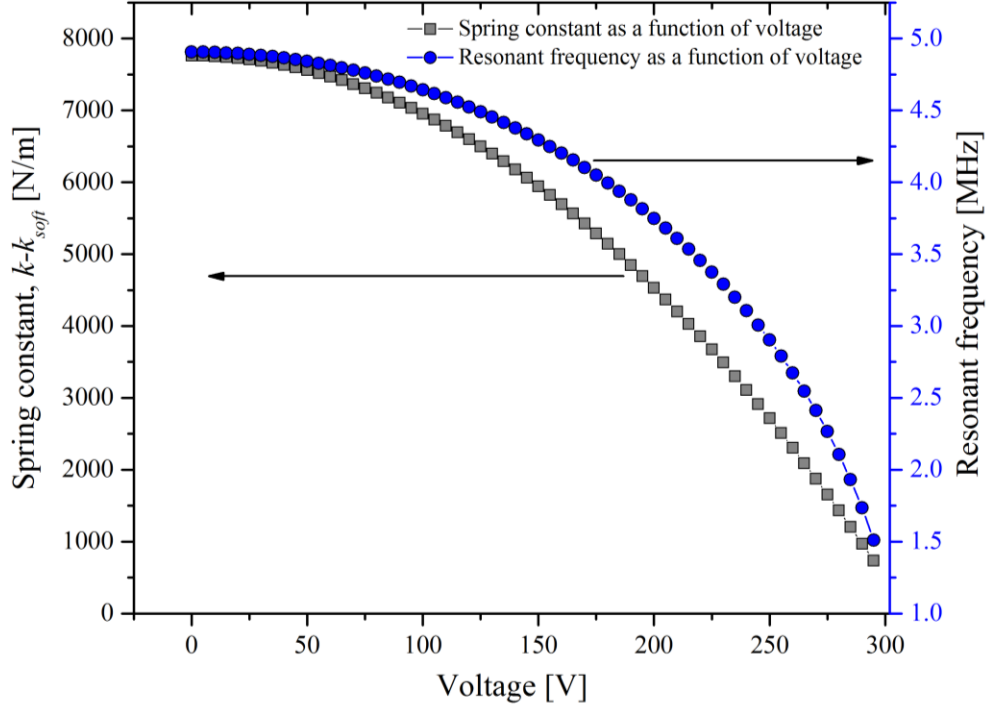
Figure 3.4. Spring constant and resonant frequency of a vibrating membrane as a function of applied DC bias for a given membrane (35 µm radius) with a given thickness (1.5 µm), and gap height (0.75 µm).

The decreasing spring constant with increasing voltage also affects the resonant behaviour of a system [21]. This can be described mathematically using the natural frequency expression of a simple mass-spring mechanical system and can be given by [45],

$$ f_r = \frac{1}{2\pi} \sqrt{\frac{k}{M}}, \qquad 3.44 $$

where f_r is the resonant frequency, M is the effective mass of the vibrating membrane with clamped edges and k is the spring stiffness of the membrane . The effective mass M can be calculated as [45]

$$ M = \rho h A \left(\frac{2\sqrt{2}}{(\lambda_a)_{mn}} \right), \qquad 3.45 $$

26

where $(\lambda_a)_{mn}$ is a constant corresponding to the shapes of different modes of membrane vibration. For a circular membrane, the value of the fundamental mode $(\lambda_a)_{mn}$ ($m = 0, n = 1$) is 3.196, where there is no nodal line (i.e. no stationary points during the vibration) but only one circular stationary line (the outer edge) [46]. The value for $(\lambda_a)_{mn}$ would be changed for different modes of vibrations and hence the mode frequency.

Substituting the spring constant (Equation 3.43) into Equation 3.44, the resonant frequencies can be calculated analytically as follows

$$f_r = \frac{1}{2\pi} \sqrt{\frac{1}{M}\left(\frac{16\pi E h^3}{3(1-v^2)R^2} - \frac{\varepsilon A V_{DC}^2}{d_0^3}\right)} \qquad\qquad 3.46$$

The resonant frequency is a function of membrane thickness, radius, membrane material, membrane mass, gap height and applied bias. This resonant frequency value increases with reducing the membrane radii. Hence, by optimizing the device radius, thickness and the gap height, a desired resonant frequency can be obtained for any particular imaging application.

In Equation 3.46, the resonant frequency is shown to be dependent upon the spring constant of the membrane. When the applied voltage is increased, due to the spring softening effect, the spring constant is decreased. As a result of that, the membrane becomes less stiff, vibrates more and the resonant frequency shifts to lower values. This behaviour is graphically shown as a function of operating voltages in Figure 3.4.

3.6 Transformation Ratio

A CMUT device converts electrical energy into mechanical energy/acoustic energy and vice versa. In transmitting mode, the deflection of a membrane generates acoustic waves and thus converts the electrical energy into acoustic energy. In receiving mode, the vibration of a membrane, caused by an external pressure wave, is detected as an alternating current and thus converts the acoustic energy into electrical energy. The energy conversion from one form of energy into another form is represented by a transformer with a transformation ratio " n ".

In transmitting mode, an ac and DC bias is applied between the electrodes. This causes the vibration of the membrane and changes the transducer capacitance. Assuming, the membrane with thickness h is separated from the bottom electrode by an initial distance d_0 and the thickness of the insulating layer is d_i, as shown in Figure 3.5.
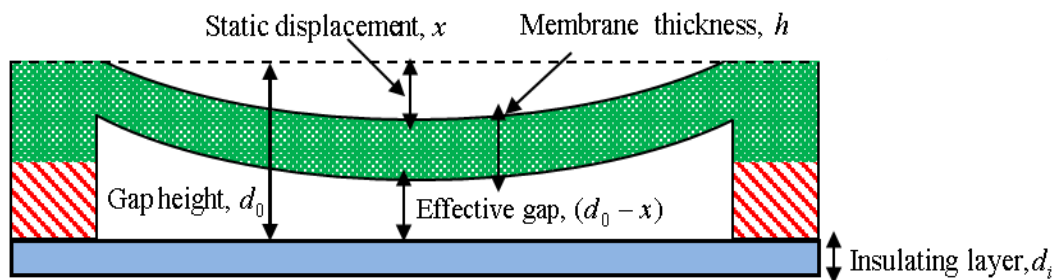
Figure 3.5. A schematic diagram of a CMUT, illustrating the membrane thickness h, initial gap height d_0 and insulating layer d_i.

The total capacitance between the top and bottom electrode can be found by taking into account all the capacitances associated with the membrane thickness, gap

height and insulation thickness. This could be calculated by taking Equation 3.16 and finding the overall series capacitance along with the membrane thickness:

$$C_T = \frac{\left(\dfrac{\varepsilon_0 \times \varepsilon_i}{\varepsilon_0 d_i + \varepsilon_i d_0}\right) \times \dfrac{\varepsilon_m}{h}}{\left(\dfrac{\varepsilon_0 \times \varepsilon_i}{\varepsilon_0 d_i + \varepsilon_i d_0}\right) + \dfrac{\varepsilon_m}{h}} \times A \qquad 3.47$$

$$= \frac{\varepsilon_0 \varepsilon_i \varepsilon_m A}{\varepsilon_0 \varepsilon_i h + \varepsilon_0 \varepsilon_m d_i + \varepsilon_i \varepsilon_m d_0} \qquad 3.48$$

The parameters used in Equation 3.47 is listed in Table 3.1

Table 3.1. Parameters used for capacitance calculation.

C_T	Total capacitance
ε_0	Permittivity of free space
ε_i	Relative permittivity of the insulating material
ε_m	Relative permittivity of the membrane material
h	Thickness of the membrane.
d_i	Thickness of the insulation layer
d_0	Initial gap height between two plates

When the membrane deflects with an amplitude, x, the effective gap height changes and hence the total capacitance

$$C_T = \frac{\varepsilon_0 \varepsilon_i \varepsilon_m A}{\varepsilon_0 \varepsilon_i h + \varepsilon_0 \varepsilon_m d_i + \varepsilon_i \varepsilon_m (d_0 - x)} \qquad 3.49$$

The electrostatic force acting on the membrane due to an applied voltage, $V(t) = V_{DC} + V_{AC} \sin(\omega t)$, where $V_{DC} \gg V_{AC}$, can be given by

$$F_E = \frac{\varepsilon A V^2}{2(d_0 - x)^2} = \frac{\varepsilon_0 \varepsilon_i^2 \varepsilon_m^2 A V_{DC}^2}{2\left(\varepsilon_0 \varepsilon_i h + \varepsilon_0 \varepsilon_m d_i + \varepsilon_i \varepsilon_m (d_0 - x)\right)^2} \qquad 3.50$$

29

The current, charging the capacitor, is given by [39]:

$$I = \frac{d}{dt}Q = \frac{d}{dt}C(t)V(t) = C(t)\frac{d}{dt}V(t) + V(t)\frac{d}{dt}C(t) \qquad 3.51$$

$$I = C(t)\frac{d}{dt}V_{AC}\sin(\omega t) + V_{DC}\frac{d}{dt}C(t) \qquad 3.52$$

As $V_{DC} >> V_{AC}$, the capacitance can be written as $C(t) = C_{DC} + C_{AC}\sin(\omega t)$. Typically the displacement of the membrane is very small compared to the gap height and hence $C_{AC} << C_{DC}$. The current equation now takes the form:

$$I = C_{DC}\frac{d}{dt}V_{AC} + V_{DC}\frac{d}{dt}C_{AC}(t) \qquad 3.53$$

Differentiating Equation 3.49,

$$\frac{d}{dt}C(t) = \frac{d}{dt}\frac{\varepsilon_0\varepsilon_i\varepsilon_m A}{\varepsilon_0\varepsilon_i h + \varepsilon_0\varepsilon_m d_i + \varepsilon_i\varepsilon_m(d_0 - x)} \qquad 3.54$$

$$= -\frac{\varepsilon_0\varepsilon_i^2\varepsilon_m^2 A}{(\varepsilon_0\varepsilon_i h + \varepsilon_0\varepsilon_m d_i + \varepsilon_i\varepsilon_m(d_0 - x))^2}\frac{d}{dt}x(t), \qquad 3.55$$

where $\frac{d}{dt}x(t) = v$ is the membrane velocity at the center, $r = 0$

$$I = C_{DC}\frac{d}{dt}V_{AC} - V_{DC}\frac{\varepsilon_0\varepsilon_i^2\varepsilon_m^2 A}{(\varepsilon_0\varepsilon_i h + \varepsilon_0\varepsilon_m d_i + \varepsilon_i\varepsilon_m(d_0 - x))^2}v \qquad 3.56$$

Equation 3.56 clearly describes the transformation of the membrane's mechanical vibration, v, into the electrical current, I. Thus, the transformation ratio (I/v) in the receiving mode of CMUTs can be written using the above expression [39]

$$n = \frac{\varepsilon_0\varepsilon_i^2\varepsilon_m^2 A}{(\varepsilon_0\varepsilon_i h + \varepsilon_0\varepsilon_m d_i + \varepsilon_i\varepsilon_m(d_0 - x))^2}V_{DC} \qquad 3.57$$

30

A simplified expression of the transformation ratio can be written as

$$n \propto V_{DC}$$
3.58

Or

$$n \propto \frac{1}{(d_0 - x)^2}$$
3.59

For a finite gap height, membrane thickness and insulating layer, the transformation ratio can be maximized by operating the transducer close to its collapse voltage. Moreover, the transformation ratio determines the transducer's sensitivity and is inversely proportional to the square of the effective gap height. For a given bias voltage, the transformation ratio can also be controlled by optimizing the effective gap height. Therefore, the bias voltage and the effective gap height have significant effect on the transformation ratio and hence to the transducer's efficiency.

3.7 Acoustic Modeling

Modeling of a vibrating CMUT membrane for acoustic radiation is challenging as it requires the coupling between the electrical domain and mechanical domain. An analytical model for acoustic pressure evaluation is discussed in the following subsection.

3.7.1 Radiation from a Plane Circular Piston

The acoustic pressure from a CMUT device was derived analytically based on a piston vibration analysis [47], where the CMUT membrane was assumed to be a piston mounted on a rigid plane boundary. The piston model was used for simplified assumptions which, for example, ignores the effect of rigid edge and includes the

31

coupling with other physical domains. A CMUT membrane can be compared to a piston when the deflection is very small comparing to the lateral membrane dimension. Assuming that, the piston has radius R , area dA and is vibrating with a displacement, x . The source is assumed to be vibrating uniformly across the surface and normal to the plane boundary with velocity, v , where $v = xe^{(j\omega t)}$. The piston model couples the electrical/mechanical domain with the acoustic domain by the piston displacement, x . The geometry, used for deriving the acoustic radiation at a point $p(r,\theta,t)$ far from the piston source, is shown in Figure 3.6.
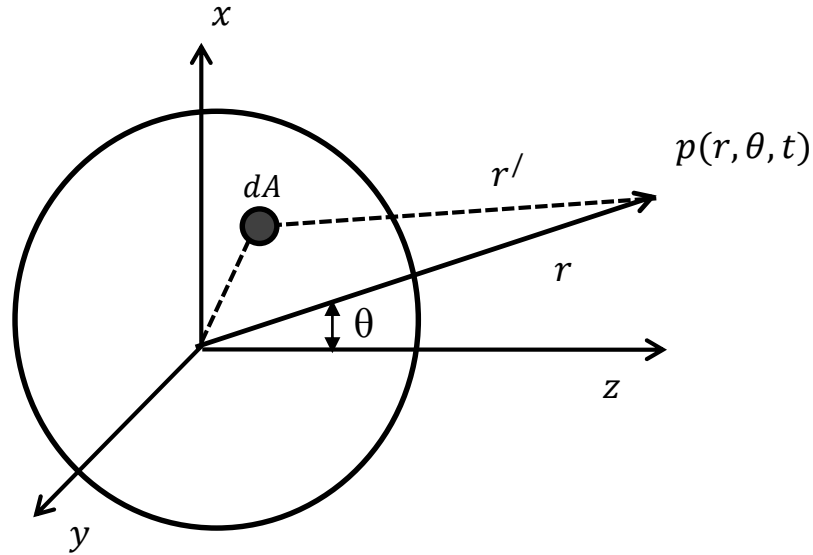
Figure 3.6. Schematic diagram of a geometry, for deriving the radiation created from a circular piston.

The acoustic pressure, p , generated by the piston source, on the axis can be written as [48]

$$p(r,\theta = 0) = 2\rho xc \left| \sin\left[\frac{1}{2} kr \left(\sqrt{1 + \left(\frac{R}{r} \right)^2} - 1 \right) \right] \right|,$$

3.60

32

where x is the piston displacement. The product of the piston density, ρ and the speed of sound, c, in a particular medium may be described as the acoustic impedance, ρc. At a distance far from the membrane, $\frac{r}{R} \gg 1$, the square root in Equation 3.60 can be simplified to

$$\sqrt{1 + \left(\frac{R}{r}\right)^2} = 1 + \frac{1}{2}\left(\frac{R}{r}\right)^2 \qquad 3.61$$

Therefore,

$$p(r, \theta = 0) = 2\rho xc \left| \sin\left\{\frac{1}{4} \times kR \times \frac{R}{r}\right\} \right|, \qquad 3.62$$

where $k = \frac{2\pi}{\lambda}$ denotes the wave number that defines the number of cycles over a specified distance and λ is the wavelength of the generated pressure wave. At a point far from the source, $\frac{r}{R} \gg 1$ and if $\frac{r}{R} \gg kR$, the pressure amplitude approaches zero asymptotically as r goes infinity.
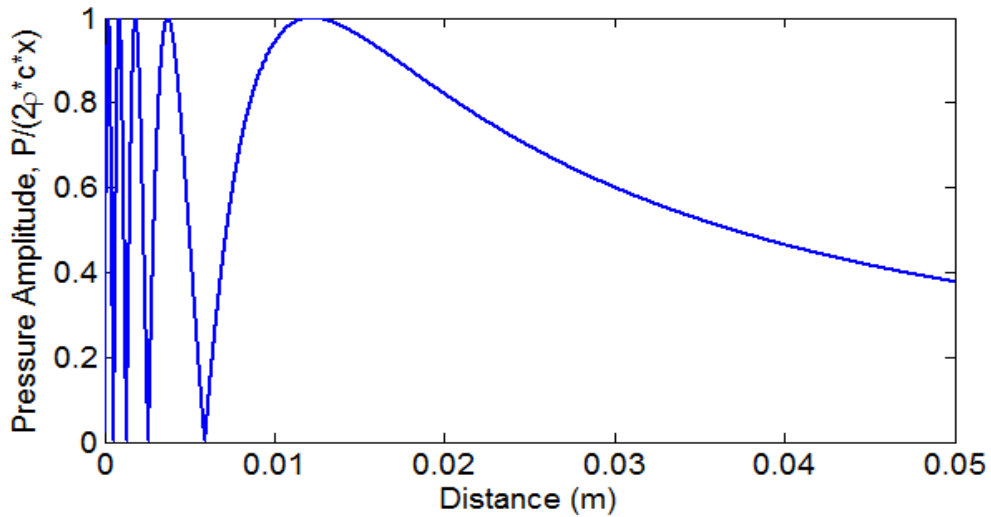
Figure 3.7. Normalized axial acoustic pressure, generated by a circular piston source, at $f = 3$ MHz with radius $R = 2.47$ mm.

Equation 3.60 is shown graphically in Figure 3.7 which illustrates the nature of the axial acoustic pressure, at positions near and far from the source. Two distinct

33

regions are clearly visible in Figure 3.7. The acoustic pressure wave has fluctuations in amplitude near the source, which is known as the "near field". In the region where the pressure wave decreases asymptotically with the distance and approaches a $\frac{1}{r}$ dependency, is referred to the "far field" region.

Typically the far field is the region of interest for most acoustic applications as the radiation pattern in the far field is found to be relatively uniform and stable. In the far field ($r \gg R$), the acoustic pressure is given by [48]

$$p(r,\theta,t) = j\frac{\rho cx}{2}kR \times \frac{R}{r} \times e^{j(\omega t - kr)}\left[\frac{2J_1(kR \sin \theta)}{kR \sin \theta}\right], \qquad 3.63$$

where the acoustic pressure contains a special term in the bracket which is known as the directivity function, DF and can be written as [48],

$$DF = \frac{2J_1(kR \sin \theta)}{kR \sin \theta} = \frac{2J_1(\pi \frac{D}{\lambda} \sin \theta)}{\pi \frac{D}{\lambda} \sin \theta} = \frac{2J_1(x)}{x} = 1 - \frac{x^2}{8} \qquad 3.64$$

where J_1 is the first order Bessel function, D is the piston length, λ is the wavelength of the generated wave, θ is the angle from an axis perpendicular to the piston's center where the sound pressure is measured (see Figure 3.6).

The directivity function gives a measure of how directional the transmitted sound wave is. The more directional a wave is, the more acoustic power is concentrated into a preferred direction. Due to this directivity function, the acoustic radiation pattern in the far field gives different values in different directions. The generated acoustic

pressure wave becomes more directional when the directivity function, DF approaches to unity as θ goes to zero.

A relationship between the directivity function and the piston length and operating frequency can be made using Equation 3.64.

$$DF = 1 - \frac{1}{8}\left(\pi\frac{1}{\lambda}\sin\theta\right)^2 \times D^2,$$ 3.65

And $$DF = 1 - \frac{1}{8}\left(\pi\frac{D}{c}\sin\theta\right)^2 \times f^2,$$ 3.66

This implies that by employing a large transducer (i.e. using numerous devices), as shown in Equation 3.65, a sharp, directional beam with a high acoustic power can be obtained. The similar result can also be achieved by operating a transducer at higher frequency (see Equation 3.66).

To have a better understanding of the characteristics of a CMUT, a finite element modeling was performed which is discussed in the following section. The analysis from the analytical method and the numerical finite element method will be used to design and optimize the CMUTs and will be fabricated.

3.8 Finite Element Modeling

Numerical based solutions (e.g. finite element modeling) are the most widely used modeling tool for designing and analyzing MEMS devices. Finite element analysis can give more accurate estimation of design, optimization and performance evaluation of MEMs transducers. Researchers have used finite element modeling (FEM) to accurately model CMUT devices, based on parallel plate capacitor and piston radiator

models [47]. A finite element modeling method is presented in the following subsections.

3.8.1 Electrostatic Finite Element Model

A finite element model of a single CMUT was constructed using COMSOL Multiphysics simulation software. The 3-D model consisted of a circular polysilicon membrane (top electrode) suspended over a silicon substrate (bottom electrode). The top electrode was separated from the bottom electrode by an air gap. A silicon nitride layer was introduced on top of the silicon substrate. The boundary conditions in the model included clamping the edge of the CMUT membrane and allowing the top membrane to be free to vibrate. The membrane was assumed to be flat initially and the edge curvatures were ignored to simplify the structure. The model used an electromechanical interface, which combined the solid mechanics and electrostatics to model the deformation of the electrostatically actuated membrane. Electrical potential (DC bias) was applied to the top electrode and the silicon substrate was grounded. No external pressure was applied on the membrane surface.

3.8.1.1 Static Analysis

The static simulations were performed to observe the nonlinear behaviour of a CMUT device under an applied bias. A fixed DC bias was applied on the membrane to model the membrane deflection as a function of static bias. The physical parameters and their values, used in FEM model, are listed in Table 3.2.

Table 3.2. CMUT Parameters for static FEM model

Parameters	Value with unit
Polysilicon membrane thickness	1.5 μm
Air gap height	0.75 μm
Silicon nitride thickness	0.6 μm
Density of polysilicon membrane	2320 kg/m^3
Polysilicon Poisson's ratio	0.22
Polysilicon Young's modulus	160 GPa
Permittivity of free space	8.854×10^{-12} F/m
Temperature	20^0 C

When an electrical potential is applied, the membrane undergoes an electric displacement due to the force caused by the applied voltage. The maximum displacement of the membrane clamped at the edge occurs at the center which can be seen in Figure 3.8. The displacement was also found to be higher for larger membranes.
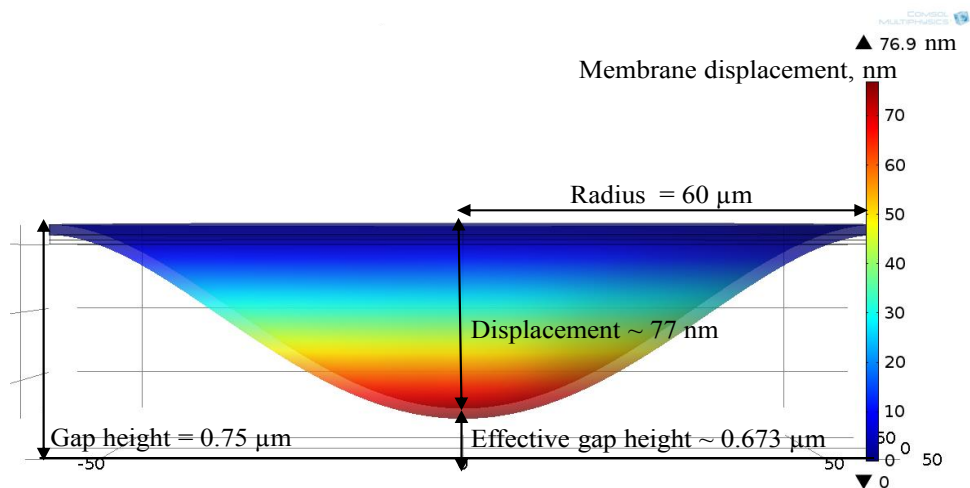
Figure 3.8. Static displacement of a polysilicon membrane (60 μm radius), with the substrate grounded and a 10 V DC bias applied to the membrane.
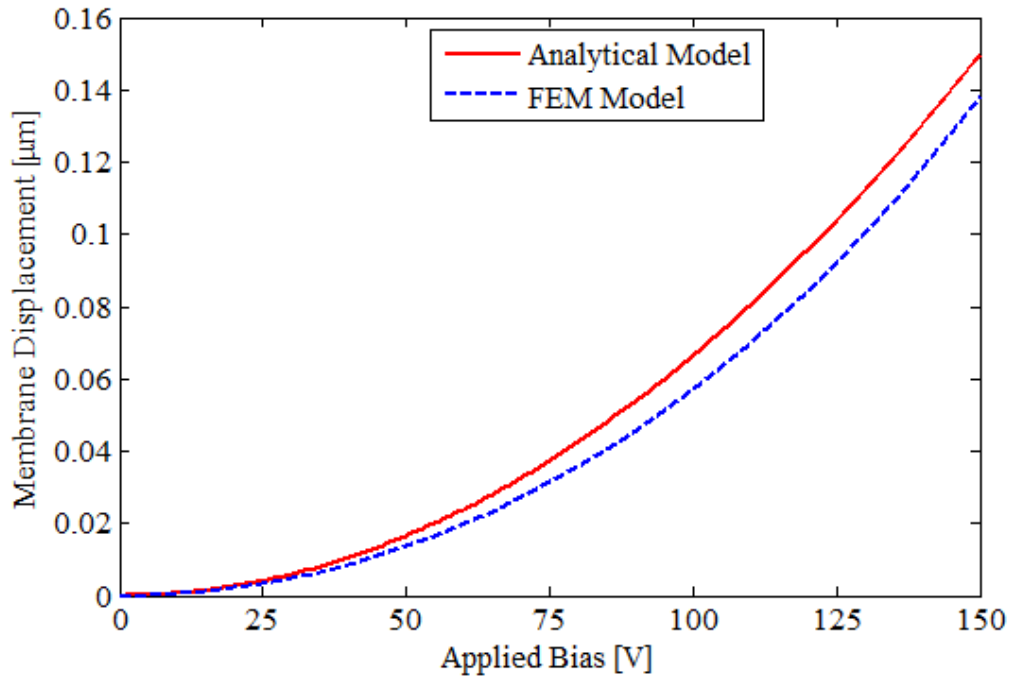
Figure 3.9. Analytical and FEM static deflection of a single CMUT device (40 μm radius) as a function of applied bias.

The maximum displacement under various DC bias were investigated by conducting the electrostatics simulations and are shown in Figure 3.9. The applied voltages for simulation were chosen to avoid membrane instability at the collapse voltage. The maximum displacement was also calculated from an analytical parallel plate model using Equation 3.39. A comparison was made between the analytical and finite element displacement of a CMUT device and is shown in Figure 3.9.

In both cases, the electrostatic force increased with an increasing bias voltage and therefore the membrane deflection also increased. However, the analytical displacement showed a slightly greater amplitude than the FEM model, especially with increasing voltages. The deviation could be the result of the simplifications made in the analytical model, which, for example, does not consider the electromechanical coupling

between the electrical and the mechanical domain or the prominent nonlinearity close to collapse voltage.

3.8.1.2 Frequency Analysis

Electromechanical Eigen frequency simulation was performed to investigate different natural vibration modes of a CMUT membrane. The Eigen frequency analysis computes natural vibration modes of a structure. The 3D shapes of a membrane with 40 µm radius at different vibration modes are illustrated in Figure 3.10. The fundamental vibration mode gave the maximum center displacement. The other modes had non-uniform membrane shapes and would therefore generate a non-uniform pressure wave.
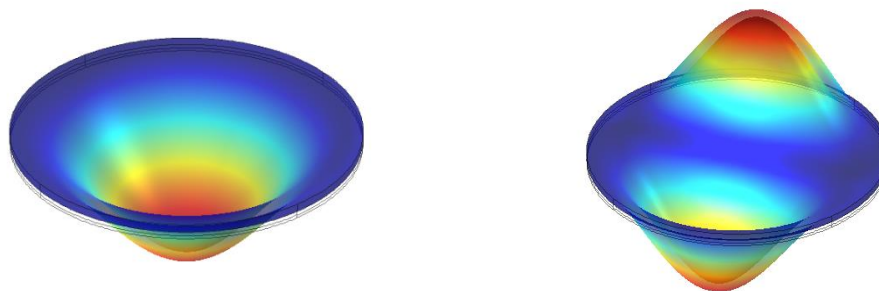
(a) (0,1) vibration mode at 3.74 MHz   (b) (1,1) vibration mode at 7.76 MHz

Figure 3.10. The simulated natural vibration modes of a 40 µm radius CMUT device with a 10 V DC bias applied to the membrane. The device physical parameters are given in Table 3.2.

The fundamental resonant frequencies of different membrane radii were determined using COMSOL Eigen frequency simulation. The resonant frequency was also calculated using previously mentioned analytical model and using the parameters listed in Table 3.2. A comparison was made between the analytical and FEM results.

This comparison is shown in Figure 3.11. The FEM results showed a close agreement with that of the analytical model for all devices except for those with extremely large radii. The small differences for large devices may be attributed to some of the simplified assumptions made in the analytical model.
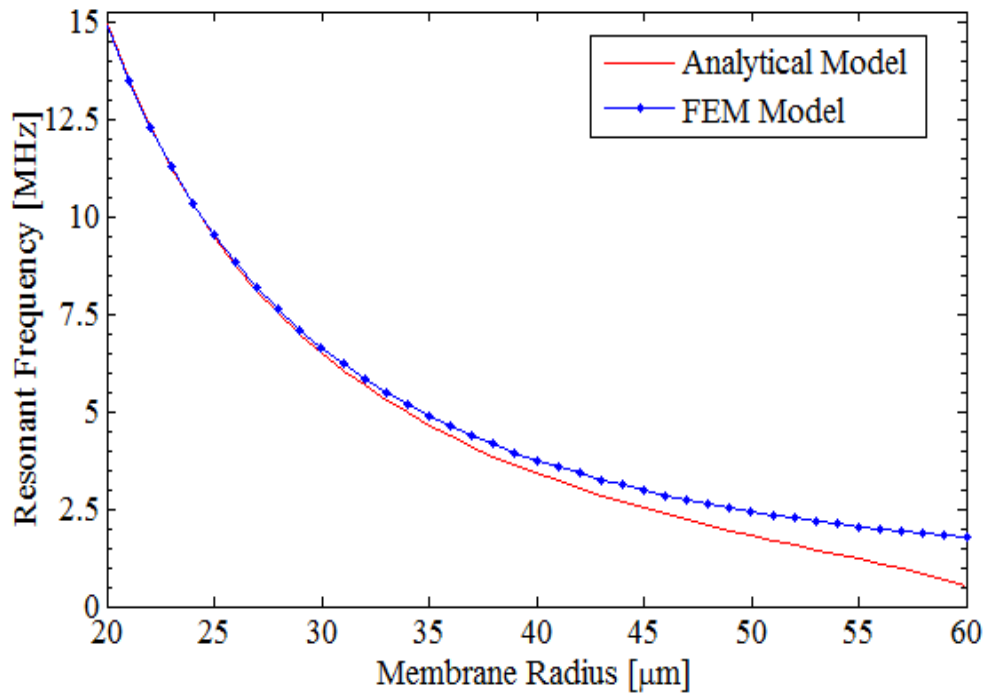
Figure 3.11. The analytical and FEM fundamental resonant frequencies as a function of membrane radii, biased with a 10 V DC.

3.8.1.3 Time Dependent Analysis

With the same geometry and boundary conditions as mentioned previously in the discussion of the static FEM model, electromechanical time dependent simulations were performed using COMSOL Multiphysics FEM software. An alternating voltage (ac) signal was superimposed on a DC bias and then was applied to the membrane. The transient response of an actuated membrane is shown in Figure 3.12, where the membrane was actuated by a 14 V, 1 MHz ac voltage, biased at 90 V DC. The static

displacement of a 40 µm radius membrane was found to be 45 nm. The ac peak to peak

displacement was found to be 31 nm, when operated at 1 MHz.
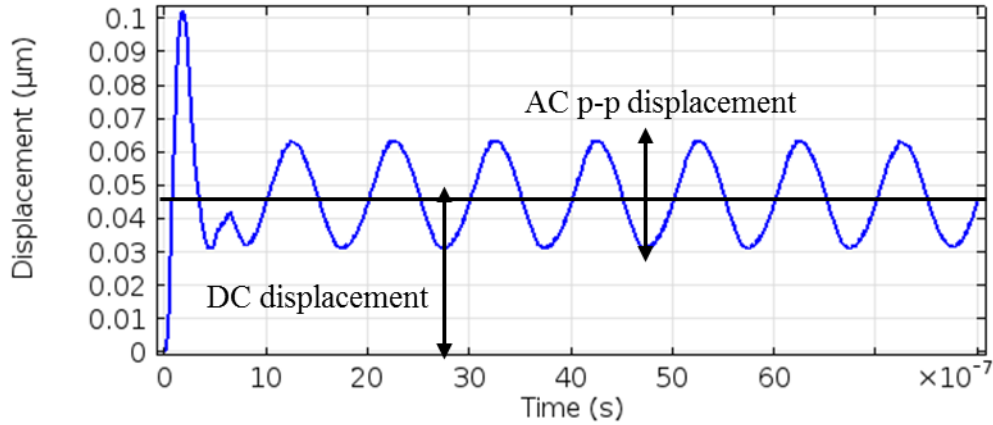
Figure 3.12. Transient response of a CMUT membrane with 40 µm radius, excited by a 14 V, 1 MHz ac voltage, biased at 90 V DC. The physical parameters for this device simulation are listed in Table 3.2.

The membrane vibration can be written as [49]

$$w = \frac{\Delta w}{2} \, sin(\omega t + \phi) \qquad\qquad 3.67$$

and membrane acceleration

$$a = -\omega^2 \frac{\Delta w}{2} \, si\,n(\omega t + \phi), \qquad\qquad 3.68$$

where Δw is the ac peak to peak displacement, $\frac{\Delta w}{2}$ is the vibration amplitude, ω is the

operating frequency and ϕ is the initial phase angle.

It was found that the vibration amplitude, $\Delta w/2$ for a fixed DC bias increased

as the ac voltage was increased, until it reached to collapse region. It was also found

that operating the transducer at higher frequencies, but still below the resonant

frequency, increased the vibration amplitude and hence the acceleration. The static

displacement, vibration amplitude and acceleration of a 40 μm radius membrane, driven

at various frequencies, with a 90 V DC bias and 14 V ac voltage are given in Table 3.3.

Table 3.3. Displacement and acceleration of a 40 μm radius CMUT membrane at various driving frequencies with a 90 V DC bias and a 14 V ac voltage signal.

Frequency (MHz)	DC displacement (nm)	ac $_{P-P}$ displacement (nm)	Acceleration (m/s^2)
1	45	31	0.61×10^6
1.5	45	36	1.59×10^6
2	45	41	3.24×10^6
2.5	45	50	6.17×10^6
3	45	60	1.07×10^7

3.8.2 Acoustic Finite Element Model

The 2-D COMSOL acoustic simulations were performed using a pressure acoustics module in the frequency domain, to investigate the acoustic pressure field generated by a CMUT device. A model was developed for simulating single device and 1-D linear array. The model consisted of a polysilicon membrane as a source, a medium (fluid/air), a structure-medium interface (membrane surface) and a perfectly matched layer. The schematic of a CMUT device to model the generated acoustic pressure is shown in Figure 3.13.
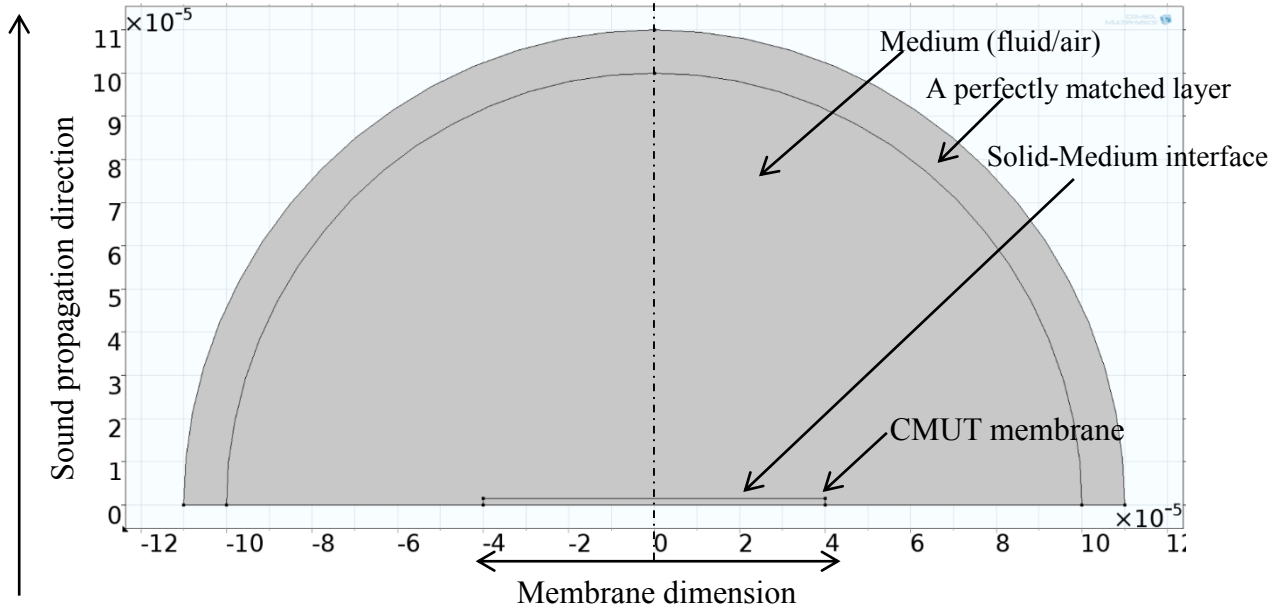
Figure 3.13. The geometry of a single membrane surrounded by water medium including a perfectly matched layer, constructed in COMSOL Multiphysics for acoustic simulations.

The propagation of sound wave in a fluid may be derived from the equation of fluid flow. The pressure of the propagating sound wave can be written as [50]

$$\frac{1}{\rho c^2}\frac{\partial^2 p}{\partial t^2} + \nabla.\left(-\frac{1}{\rho}(\nabla p - q)\right) = Q, \qquad 3.69$$

where p is the acoustic pressure field, ρ is the density of the fluid, c the speed of sound in the fluid, q and Q are the acoustic sources. The above wave equation can be solved in the frequency domain and the acoustic pressure component can be written using complex variables

$$p = p(x)e^{j\omega t}, \qquad 3.70$$

where $p(x)$ is the spatial pressure. Substituting Equation 3.70 into 3.69, the time dependent wave equation becomes the well-known Helmholtz equation

43

$$\nabla.\left(-\frac{1}{\rho}(\nabla p - q)\right) - \frac{\omega^2}{\rho c^2}p = Q \qquad\qquad 3.71$$

The CMUTs were assumed to be operated in water-immersion mode. A spherical domain of water was considered around the CMUT device. The radius of the water domain was set to 5 cm which satisfies the far field condition given by [51]

$$NF = \frac{D^2}{4\lambda}, \qquad\qquad 3.72$$

where NF is the near field boundary, D is the total length of the transducer, λ is the wavelength ($\lambda = cf$), c is the speed of sound in water, and f is the operating frequency. The model includes a perfectly matched layer at the outer boundary of the water domain, to absorb all the outgoing waves and thus eliminate reflections at the interface. The width of the matched layer was set to be 5λ, which was wide enough to absorb the outgoing waves. A normal acceleration was applied to the solid-medium interface (i.e. CMUT surface) to couple the electromechanical domain with the acoustic domain. The normal acceleration, $a_{membrane}$ can be given by [50]

$$a_{membrane} = \frac{d^2 w(t)}{dt^2} = n\left(\frac{1}{\rho}(\nabla p)\right) \qquad\qquad 3.73$$

where n is the unit normal vector, $a_{membrane}$ is the membrane acceleration and $w(t)$ is the vibration amplitude. The normal acceleration was calculated from the electromechanical time dependent simulation (see Figure 3.12 and Table 3.3). Due to the applied acceleration, the CMUT membrane vibrates and generates an acoustic pressure wave which is directly proportional to the vibration amplitude.

In this model, a boundary condition was applied at the edge of the CMUT device, where the normal velocity was set to zero.

$$n\left(\frac{1}{\rho}(\nabla p)\right) = 0 \qquad\qquad 3.74$$

After applying all the boundary conditions, the acoustic pressure can be calculated using the Helmholtz equation and can be given by

$$\nabla.\left(-\frac{\nabla p}{\rho}\right) - \frac{\omega^2}{\rho c^2}p = 0 \qquad\qquad 3.75$$

Typically, the CMUTs are fabricated in large arrays and all the devices are actuated simultaneously to get a larger acoustic pressure. Therefore, a 1-D CMUT array with 55 single devices, with a 10 µm spacing between two individual devices, was simulated to investigate the generated acoustic pressure distribution. The generated acoustic pressure from this array and the variation in acoustic pressure with distance is shown in Figure 3.14 and Figure 3.15 respectively. The parameters used in the acoustic simulations are listed in Table 3.4.

Table 3.4. CMUT Parameters used in acoustic simulation

Parameters	Value with unit
Polysilicon membrane radius	40 µm
Membrane thickness	1.5 µm
Speed of sound in acoustic medium	1500 m/s
Acoustic medium density(water)	1000 kg/m^3
Radius of acoustic medium	5 cm
Inter element spacing	10 µm
Operating frequency	3 MHz
No. of devices in an array	11-95
Temperature	20^0 C
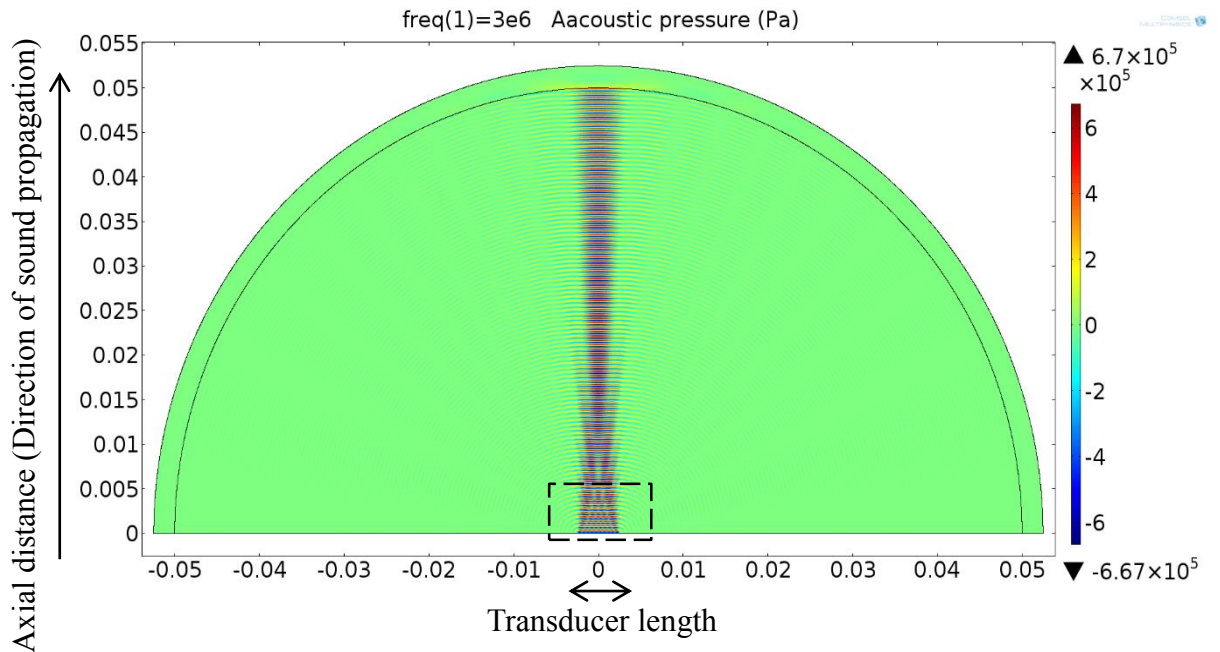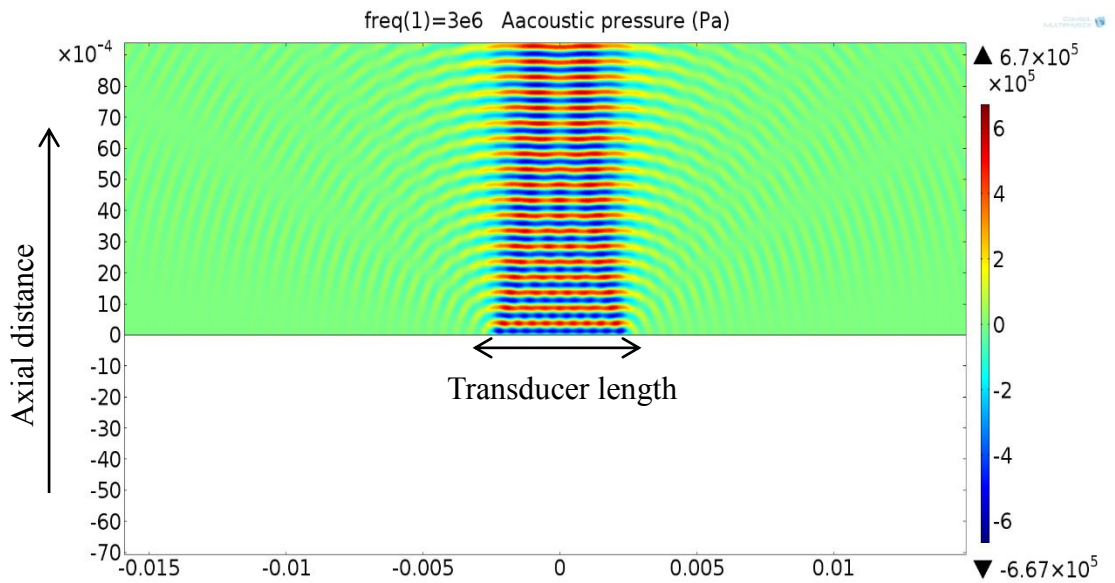
Figure 3.14. (a) The acoustic pressure distribution in water, generated by a 1-D array, with 55 single devices in a row and operating at 3 MHz frequency. (b) Enlargement of the acoustic pressure distribution of a small area indicated by the dashed line box in (a). The physical device parameters used in the acoustic 2-D simulation are given in Table 3.4.
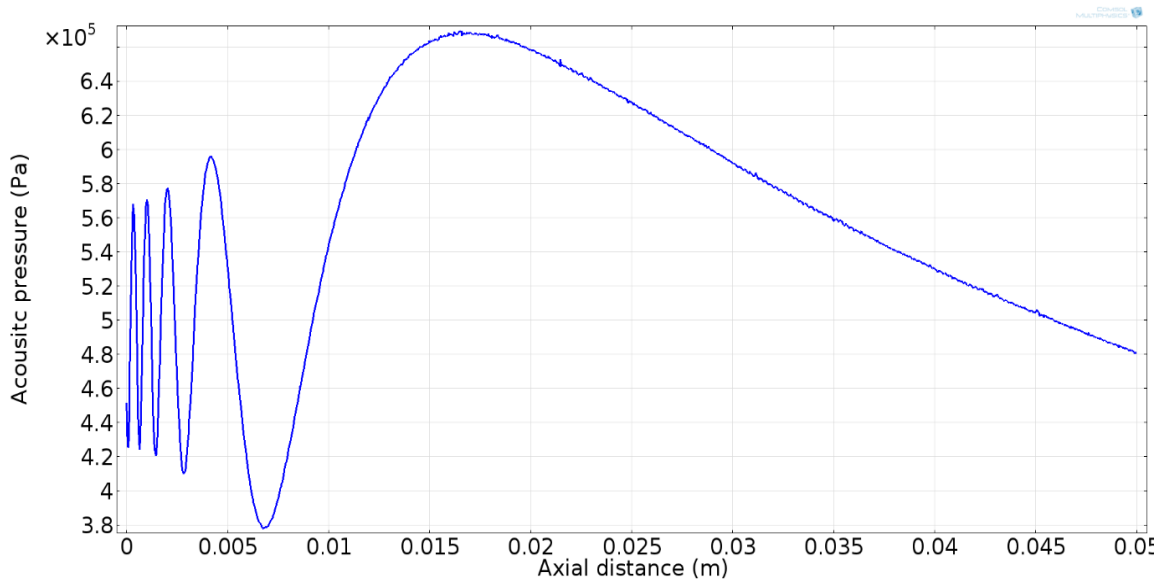
Figure 3.15. The variation of acoustic pressure with axial distance (direction of sound propagation), generated by a 1-D transducer array with 55 devices in a row and operating at 3 MHz frequency.

In Figure 3.15, the acosutic pressure near the source has fluctuations in pressure amplitude. This region is commonly known as the "Near field" region. Just beyond the near field region, the sound pressure is relatively uniform (between 15-20 mm), after which the pressure decreases asymptotically with increasing distance from the array. This later region is referred to the "Far field" region [52].

The directivity pattern of the generated sound pressure is important to be investigated as the directivity pattern gives a measure of how directional the transmitted sound wave is. From Equation 3.65, the directivity of a beam was found to be dependent on the transducer length, the operating frequency and the speed of sound in a particular medium. By conducting COMSOL pressure acoustic simulations, the beam directivity pattern and sound pressure level of different 1-D CMUT arrays were investigated.

47

(a)   (b)
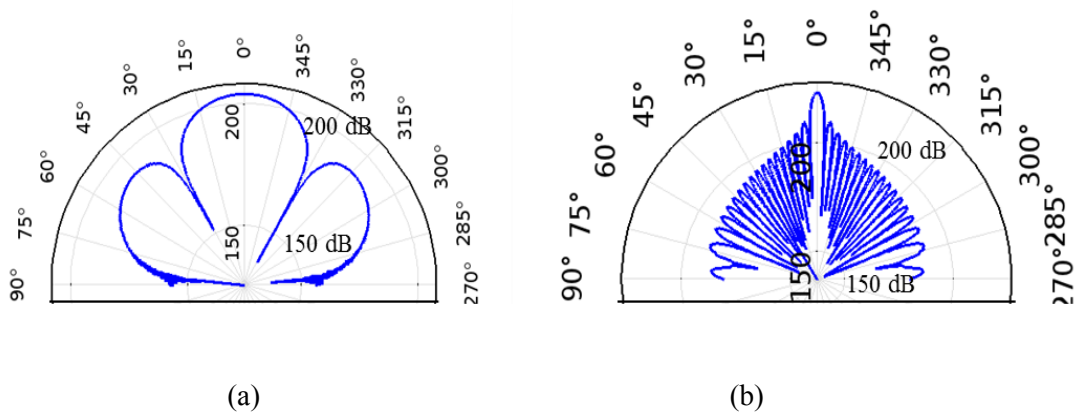
Figure 3.16. The simulated angular beam directivity pattern showing the sound pressure level (dB) for two different arrays (a) 11 devices (b) 95 devices, operating at 3 MHz frequency.
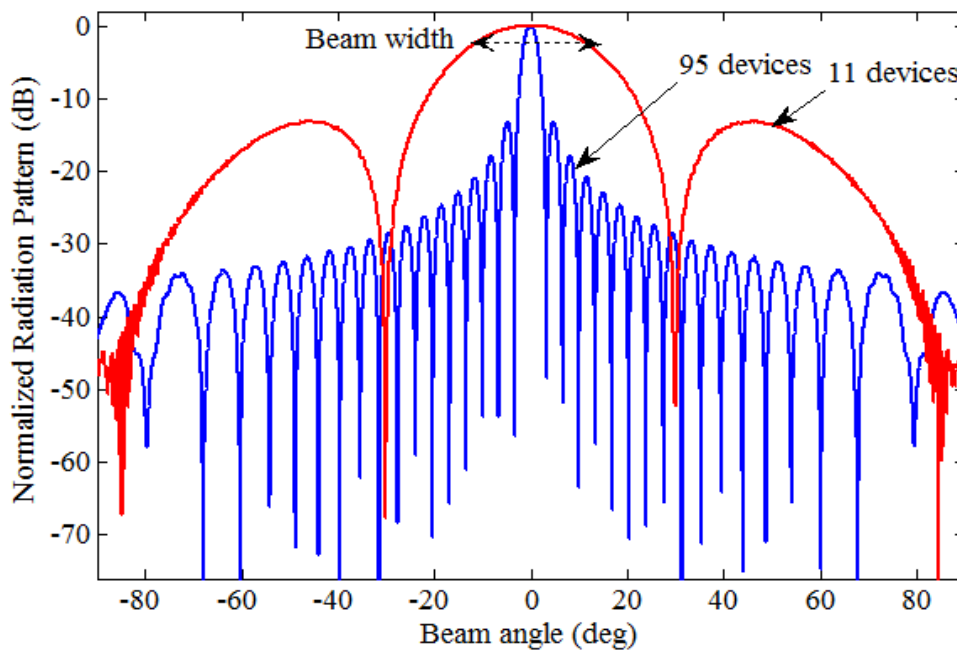
Figure 3.17. The simulated radiation pattern (sound pressure level) at the far field as a function of beam angle of two different arrays: 11 devices and 95 devices, operating at 3 MHz frequency.

The simulated angular beam directivity pattern of two 1-D arrays with different

transducer lengths (D) is shown in Figure 3.16. The directivity is expressed as the

angular separation at the point where the peak radiation decreases by 50% or -3 dB from the peak value of the main beam. This angle is known as half power beamwidth (HPBW) or -3 dB beamwidth. The -3 dB beam width for the 11 device array (length =0.98 mm) was 25.9^0 and for the 95 device array (length=4.94 mm) it is much smaller at only 3^0, as shown in Figure 3.17. It can be seen from Figure 3.17 that the radiation pattern of the 95 device array transducer is more directional and has more concentrated power into the center of the main lobe. The -3 dB beam width and corresponding maximum sound pressure level were extracted from the acoustic simulations and are plotted in Figure 3.18. The acoustic pressure P is normally expressed on a logarithmic scale (dB) (see Equation 3.76) and can be calculated using Equation 3.63 or Equation 3.75,

$$\text{Sound Pressure Level} = 20 \log_{10} \frac{P}{P_{ref}} \, dB \qquad 3.76$$

where P_{ref} is the reference pressure in water with a value $P_{ref} = 1 \ \mu Pa$
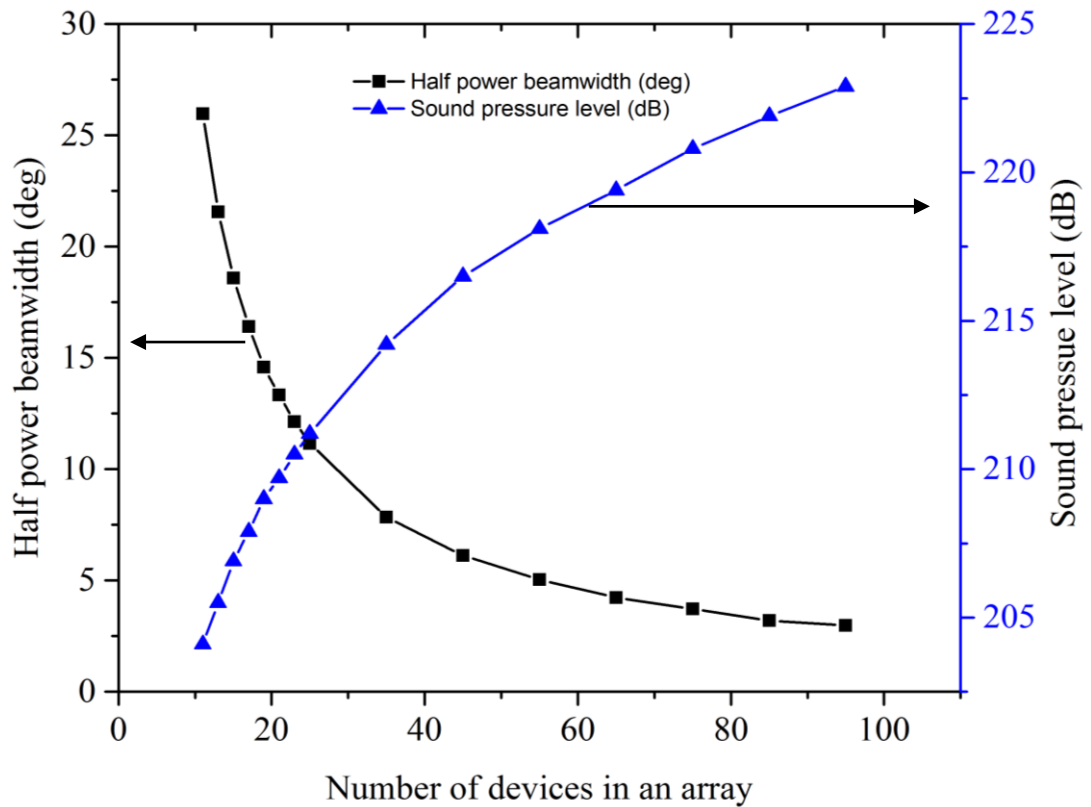
Figure 3.18. The half power beamwidth (-3 dB) and sound pressure level (dB) for arrays of different transducer lengths, operating at 3 MHz frequency.

From Figure 3.18, it can be seen that a larger array of transducers (i.e. employing 95 devices in the array as opposed to 11 devices) results in a more directional and sharp beam. Therefore, a highly directive CMUT array with significant acoustic pressure field for imaging can be achieved by increasing the transducer array length and employing more CMUT devices in an array.

Chapter 4: Fabrication Process Flow

To ensure a successful fabrication yield, a system-level design of capacitive micromachined ultrasonic transducer (CMUT) was performed using a commercially available MEMS Pro CAD tool. Different design parameters were investigated to yield a larger acoustic signal generation, higher sensitivity, optimum resonant frequency and lower driving voltage. Based on the simulations performed in COMSOL Multiphysics (as mentioned in Chapter 3), some single devices and 1-D arrays were designed and fabricated.

4.1 Fabrication Method and Design Considerations

The CMUTs were fabricated using PolyMUMPs technology offered by MEMSCAP Inc. through CMC Microsystems. PolyMUMPs has been widely used as a fabrication technology for MEMS devices for over a decade. Different types of sensors have been fabricated using PolyMUMPs process, which include acoustic sensors, accelerometers, micro-fluidics, robotics, display technologies etc. PolyMUMPs technology is convenient and economical fabrication process for MEMS devices that offers a variety of design parameters. The PolyMUMPs process provides three polysilicon layers as the structural layers, two deposited oxide layers as the sacrificial layers, and a silicon nitride layer as an isolation between the substrate and the polysilicon layers [53]. The material layers with their thickness are given in Table 4.1.

Table 4.1. Layers name and thickness offered by POLYMUMPs

Material layer	Thickness
Silicon Nitride	600 nm
Poly 0	500 nm
First Oxide	2.0 µm
Poly 1	2.0 µm
Second Oxide	0.75 µm
Poly 2	1.5 µm
Metal	0.5 µm

From the analytical and finite element analysis, discussed in Chapter 3, it was found that a thinner membrane gives a larger signal amplitude (see 3.8.1.1), and a lower gap height provides a lower collapse voltage (see Figure 3.3). The collapse voltage and the resonant frequency, using the available design parameters from the PolyMUMPs process, were calculated using Equation 3.14 and 3.46, and are given in Table 4.2.

Table 4.2. Calculated collapse voltages of different gap heights of a membrane with radius 40 µm and thickness 1.5 µm.

Sacrificial Material	Gap Height	Collapse Voltage	Resonant Frequency
Oxide 1	2 µm	564 V	3.75 MHz
Oxide 2	0.75 µm	129 V	3.75 MHz
Oxide 1+ Oxide 2	2.75 µm	909 V	3.75 MHz

The oxide 2 layer (0.75 µm thickness), as the sacrificial layer and subsequently defining the gap height, was shown to provide lowest collapse voltage (see Table 4.2). Hence, the oxide 2 layer was used as the sacrificial layer and the poly 2 layer with 1.5

µm thickness was chosen to be used as the structural layer. A silicon nitride layer with 600 nm thickness was used to isolate the substrate from the other layers. Different device radii (ranging from 20 to 60 µm) were designed to yield resonant frequencies in the range 1-10 MHz. Single devices with radii of 20, 30, 40, 50 and 60 µm were fabricated. Two 1-D arrays with radius 40 µm were also fabricated in the same chip.

Two design configurations were employed in this work. The first configuration used the poly 2 layer as the top electrode and the heavily doped silicon surface as the bottom electrode. This particular configuration that was symbolized as "Design-B" may suffer from an electrical shorting between the top electrode and the bottom substrate due to the absence of an isolation layer. This electrical shorting could permanently damage the device. Therefore, to avoid permanent damage of this device, a 600 nm silicon nitride isolation layer was deposited onto the substrate and thus introduced another design configuration as "Design-A".

4.2 Fabrication Process

The process began with a 150 mm n-type (100) silicon wafer with a resistivity of 1-2 Ω-cm. The surface of the wafer was heavily doped with phosphorus, which was later used as the ground electrode in both designs. A 600 nm silicon nitride layer was then deposited as an electrical isolation layer using LPCVD (Low pressure chemical vapour deposition), shown in Figure 4.1 (a) and Figure 4.2 (a). A small area of the nitride layer was removed at the corner of the chip to allow contact to the substrate, which was later bonded to a contact pad [53].

A 500 nm LPCVD Polysilicon film (Poly 0) was deposited, patterned by photolithography and etched using plasma etching (see Figure 4.1 (b) and Figure 4.2 (b)). This was then followed by the deposition of a 2.0 μm LPCVD phosphosilicate glass (PSG) layer (oxide 1), shown in Figure 4.1 (c) and Figure 4.2 (c). It was then annealed at 1050^0 C for 1 hour. The PSG layer was lithographically patterned and etched using plasma etching. A 2.0 μm Polysilicon structural layer (Poly 1) was then deposited using LPCVD. Another 200 nm PSG layer was deposited over the Poly 1 layer and the wafer was then annealed at 1050^0 C for 1 hour. The annealing process dopes the polysilicon layer and considerably reduces the stress in the Poly 1 layer. The Poly 1 layer (along with the PSG layer) was then lithographically patterned and etched, shown in Figure 4.1 (d) and Figure 4.2 (d). This step allowed to form a stack of polysilicon layers which was used as an anchor for the next structural layer (see Figure 4.1 (d)).

After Poly 1 was etched, a second 0.75 μm sacrificial PSG layer (oxide 2) was deposited and annealed at 1050^0 C for 1 hour, as shown in Figure 4.1 (e) and Figure 4.2 (e). The second oxide layer was then lithographically patterned to provide a mechanical and electrical connection between the Poly 1 and Poly 2 layers as the design required and then etched using plasma etching. The second 1.5 μm Polysilicon structural layer (Poly 2) was then deposited followed by the deposition of a 200 nm PSG layer, shown in Figure 4.1 (f) and Figure 4.2 (f). The wafer was annealed at 1050^0 C for 1 hour to dope the Poly 2 layer and to reduce residual film stress. The PSG and polysilicon layer were then photo lithographically patterned and etched using plasma etching.

A 0.5 μm metal layer was deposited (only in array structures) and then patterned with a lift-off process, which provided the probing and electrical connection. The final step was to release the Poly 2 layer by removing the second sacrificial layer (oxide 2) underneath. The sacrificial release was performed by immersing the chip into 49% hydrofluoric acid (HF) for 1.5-2 minutes. This was followed by rinsing in deionized (DI) water, in alcohol to avoid stiction and was then baked in an oven at 110°C for 10 minutes [53]. The final CMUT structure of Design-A and Design-B, after sacrificial release, can be seen in Figure 4.1 (g) and Figure 4.2 (g) respectively.

(a)

(b)

(c)

(d)

(e)

(f)

(g)
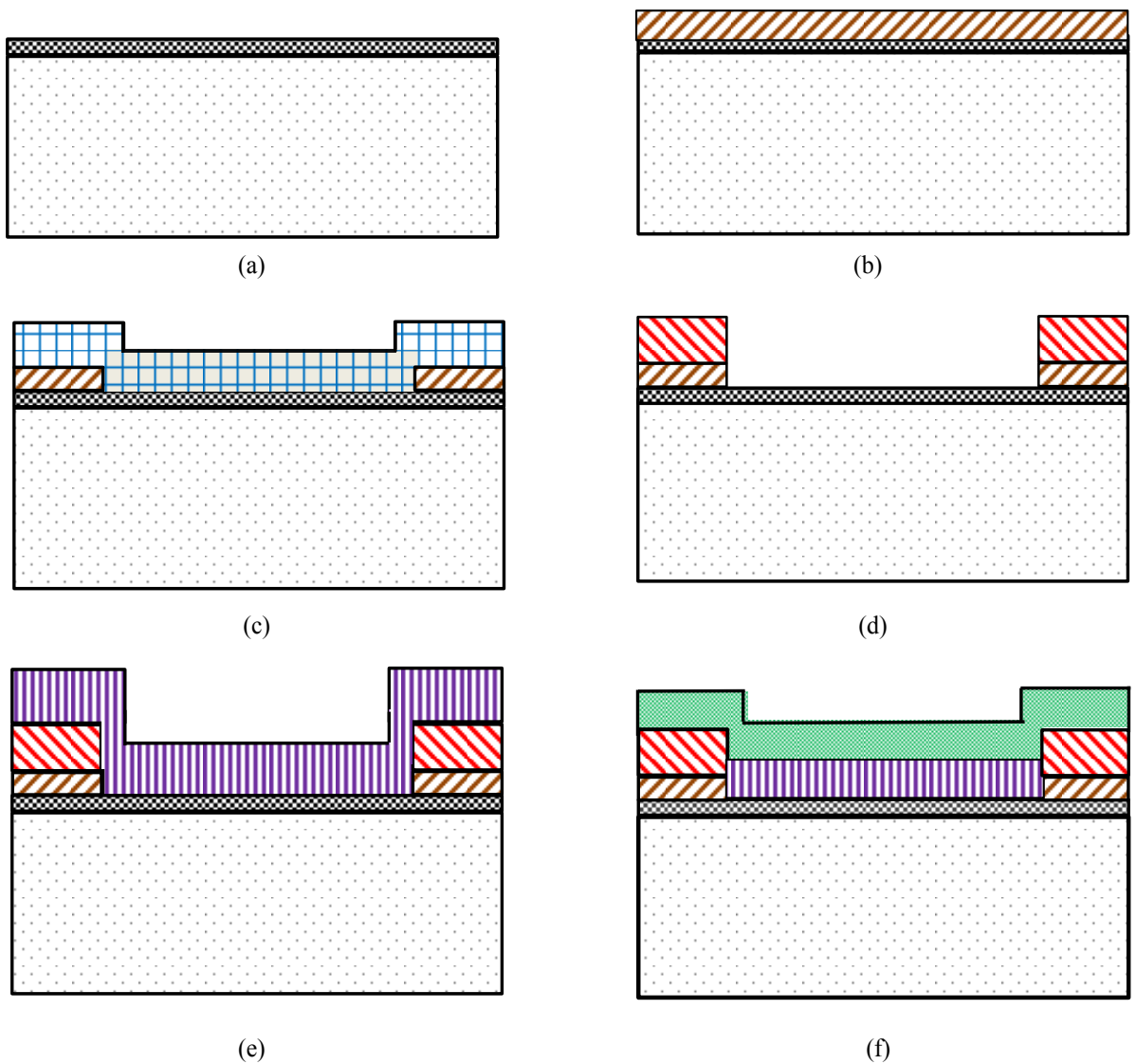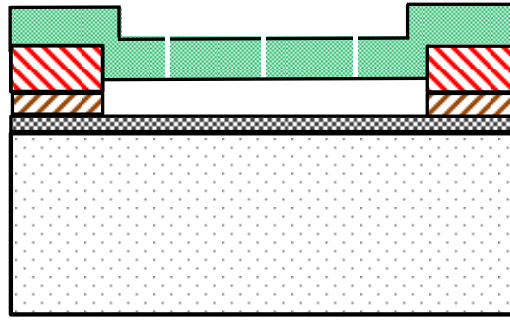
Substrate Nitride Poly 0 Oxide 1 Poly 1 Oxide 2 Poly 2

Figure 4.1. The process steps for the PolyMUMPs fabrication technology: Design-A (a) Deposition of silicon nitride layer on the doped silicon substrate as an insulating layer between the gap and the substrate. (b) Deposition of Poly 0 layer on the silicon nitride layer, patterned and etched. (c) Deposition of oxide 1 layer, patterned and plasma etched (d) Deposition of Poly 1 layer, lithographically patterned and etched. (e) Deposition of oxide 2 layer as the sacrificial layer, lithographically patterned and etched. (f) Deposition of Poly 2 layer as the structural layer (CMUT membrane). (g) Releasing the Poly 2 membrane by removing the oxide 2 sacrificial layer by immersing into 49% HF bath for 1.5-2 minutes. (Layer heights and dimensions are not in scale).

(a)

(b)

(c)   (d)

(e)   (f)

(g)
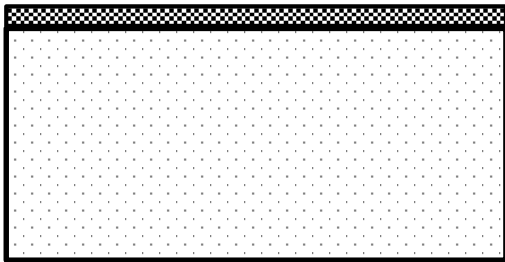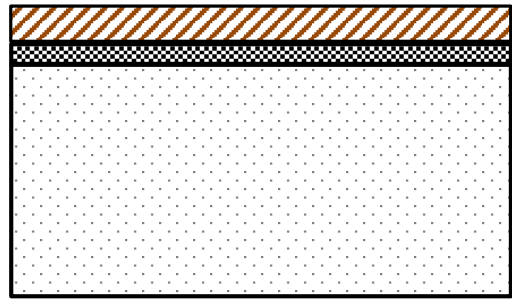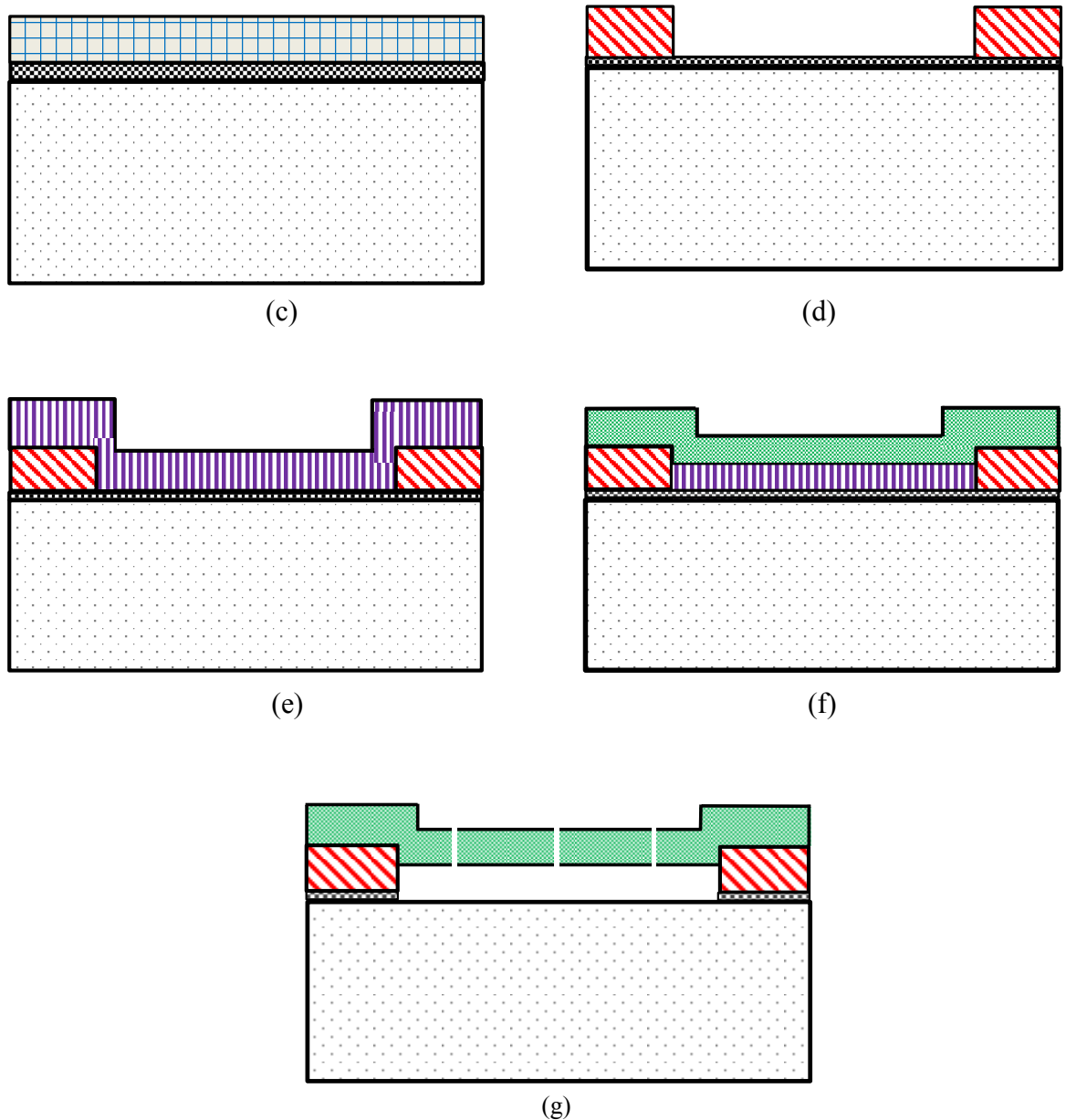
Substrate   Nitride   Poly 0   Oxide 1   Poly 1   Oxide 2   Poly 2

Figure 4.2. The process steps for the PolyMUMPs fabrication technology: Design-B (a) Deposition of a silicon nitride layer on the doped silicon substrate as an insulating layer between the top and bottom electrode. (b) Deposition of Poly 0 layer on the silicon nitride layer, patterned and removed by plasma etching. (c) Deposition of oxide 1 layer, lithographically patterned and etched using plasma etching. (d) Deposition of Poly 1 film, lithographically patterned and etched. (e) Deposition of oxide 2 layer as the sacrificial layer, patterned and etched using plasma etching. (f) Deposition of Poly 2 which is the CMUT membrane. (g) Releasing the Poly 2 membrane by removing the oxide 2 layer by immersing into 49% HF bath for 1.5-2 minutes. (Layer heights and dimensions are not in scale)

Chapter 5: Electrical and Optical Characterization of CMUTs

The electrical characterization of the fabricated CMUT devices is presented in this chapter. The key parameters that were measured are capacitance, input impedance, resonant frequency and collapse voltage. The capacitance and the electrical impedance were measured to investigate the transducer's functionality under various biasing conditions. The resonant frequency was measured to study the CMUT's operating frequency range. To avoid the mechanical breakdown of a membrane due to a high electric field, the collapse voltage was investigated. The optical characterization of the CMUT devices which includes the visualization and analysis of structural vibrations is also described in this chapter.

5.1 Electrical Characterization

In this work, two CMUT designs were fabricated. In the first design (Design-A), the membrane support was slightly higher than the second design (Design-B), resulting from an extra silicon nitride layer, as shown in Figure 5.1. This resulted a marginally higher gap at the edge of Design-A, while maintaining the same effective membrane dimension as Design-B. The effective membrane diameters for the two designs are shown in Figure 5.1. The electrical characterization results using Design-A and Design-B CMUT devices are presented in the following sections.
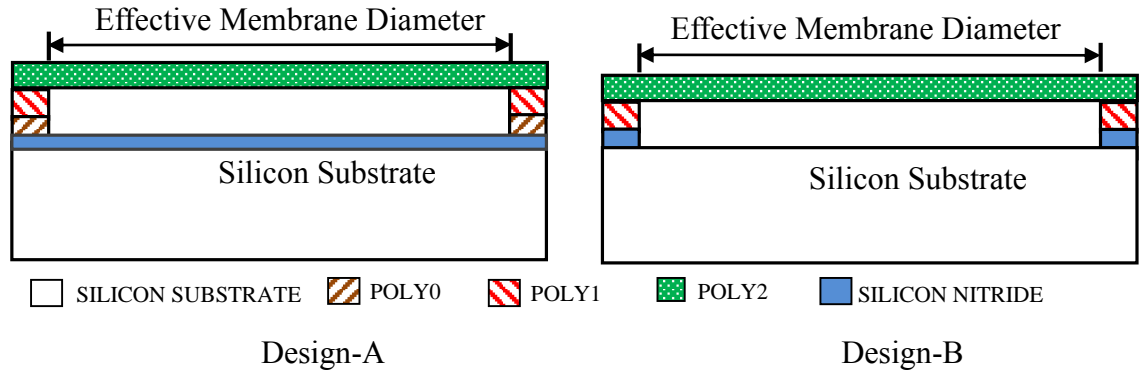
Figure 5.1. Schematic view of a PolyMUMPs fabricated CMUT: (a) Design-A (b) Design-B (not in scale)

5.1.1 Capacitance without Bias

A CMUT is a variable capacitor that changes its capacitance with an applied bias. Hence, the capacitance of a CMUT device is important to measure both with and without an applied bias. At first, the capacitance was measured at zero bias voltage for Design-A and Design-B devices of several areas. The capacitance measurement was performed using an Agilent 4284A Precision LCR meter. A small 50 mV ac voltage signal was applied to enable the capacitance measurement.

The voltage was applied to the polysilicon 2 layer which was the top electrode and the substrate as the bottom electrode was grounded. The capacitance measured using the LCR meter included the membrane capacitance, and the parasitic elements associated with the interconnecting and the metal pad. Even though the membrane dimension of Design-A and Design-B were the same, Design-A devices had higher parasitic elements as discussed and shown in detail in Section 4.2. Therefore, Design-A devices had a higher effective area including both the membrane and parasitic elements than Design-B devices, for a given radius of device.
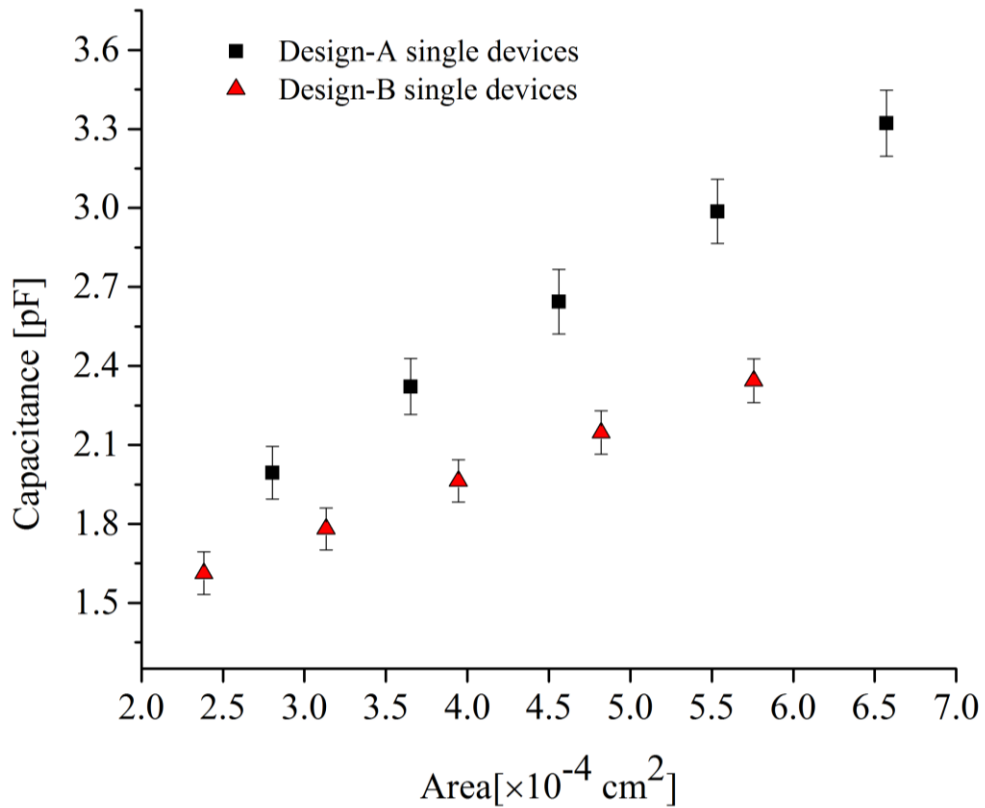
Figure 5.2. Capacitance of Design-A and Design-B CMUT single devices as a function of area.

The measured capacitance of five single devices (Design-A) as a function of their area is shown in Figure 5.2, where the capacitance changes linearly with the area. Design-B devices also showed a linear relationship between the capacitance and their area, as shown in Figure 5.2. A parasitic capacitance of 1.8 pF (Design-A) and 1.58 pF (Design-B) was found in the experimental data, which was extracted from the intercept at the y axis of Figure 5.2. The error bars were calculated from the standard deviation of five sets of experimental data measured on the same devices.

5.1.2 Capacitance with Bias

In order to investigate the basic functionality of a PolyMUMPs fabricated CMUT device, the capacitance under various bias voltages was measured. An Agilent

Precision Impedance Analyzer 4294A was used to measure the capacitance of single devices and 1-D arrays. The impedance analyzer was used for this measurement as it provided a broader frequency range (40Hz-110MHz) than the LCR meter (20Hz-1MHz). A custom designed bias-T was used to superimpose the ac and DC signals and then applied to the CMUT which was in a test fixture. The test fixture was used to interface the packaged device to the impedance analyzer through BNC connectors. The maximum DC voltage limit of the bias-T was 100 V and it had a frequency range 500 kHz-15 MHz. In this experiment, a 50 mV, 1 MHz ac voltage signal was applied using the Precision Impedance Analyzer. A Keithly 237 high voltage source was employed as the DC source. The DC bias was swept from 0 V to 70 V in 2 V increments. A diagram of this experimental setup is shown in Figure 5.3.
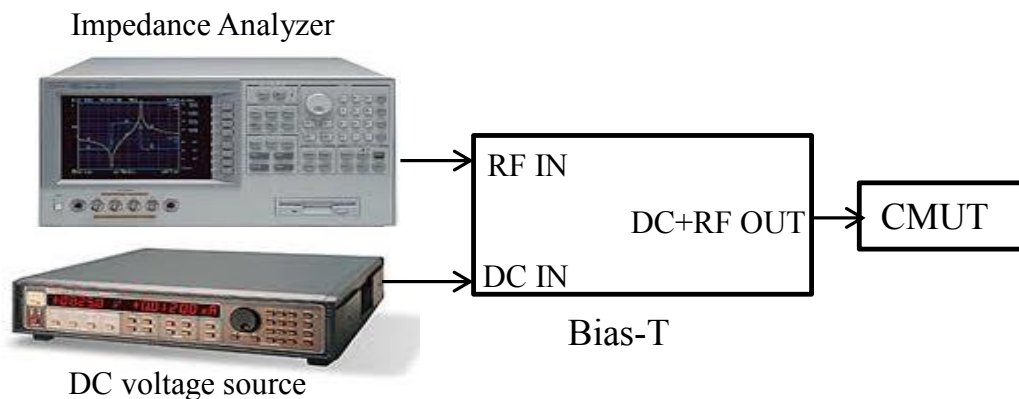
Figure 5.3. Experimental set up for capacitance measurement, performed at room temperature.
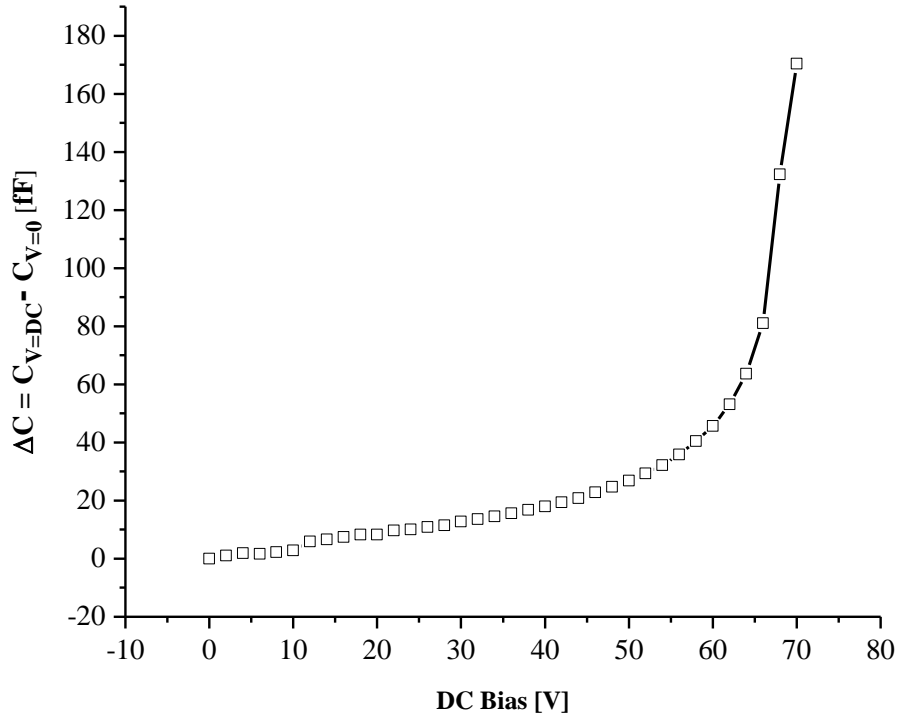
Figure 5.4. Differential capacitance as a function of DC bias of a 60 μm radius membrane CMUT. A 50 mV, 1 MHz ac voltage was superimposed on the DC Bias.

The frequency and amplitude of the ac signal was chosen to be far from the device resonant frequency to obtain a "static-like" capacitance with minimal vibration. The capacitance of a CMUT device with 60 μm membrane radius (Design-A) was measured at each voltage step, plotted as a function of DC bias and is illustrated in Figure 5.4. This 60 μm membrane exhibited a capacitance change of 170 fF from 0 V to 70 V.

The capacitance of a CMUT device can be expressed using Equation 3.3 which is repeated here for the convenience of the reader.

$$C = \frac{\varepsilon A}{d_0 - x},$$

where ε is the dielectric permittivity of air, A is the membrane area, d_0 is the initial air gap height and x is the vertical membrane displacement under an applied bias.

When a DC bias is applied across the capacitor, the membrane deflects and the total gap height is reduced. The reduction in gap height increased the capacitance of the 60 μm radius membrane, resulting from the increased membrane deflection. The standard deviation, measured from averaging 801 measurement points (provided by the impedance analyzer), was found to be small ~0.063 fF and could be the result of equipment noise. The effect of parasitic elements on the membrane capacitance due to the wire bonding, soldered connections and the test fixture was assumed to be independent of a bias voltage or frequency.

The capacitance of two 1-D arrays (Design-A and Design-B) was also measured using the impedance analyzer. The DC bias was again swept from 0 V to 70 V but with a 5 V step size. Each array consisted of 22 single devices connected to each other with a metal layer; each single device had a membrane of 40 μm radius. The capacitance change of two 1-D arrays as a function of applied DC bias is shown in Figure 5.5.
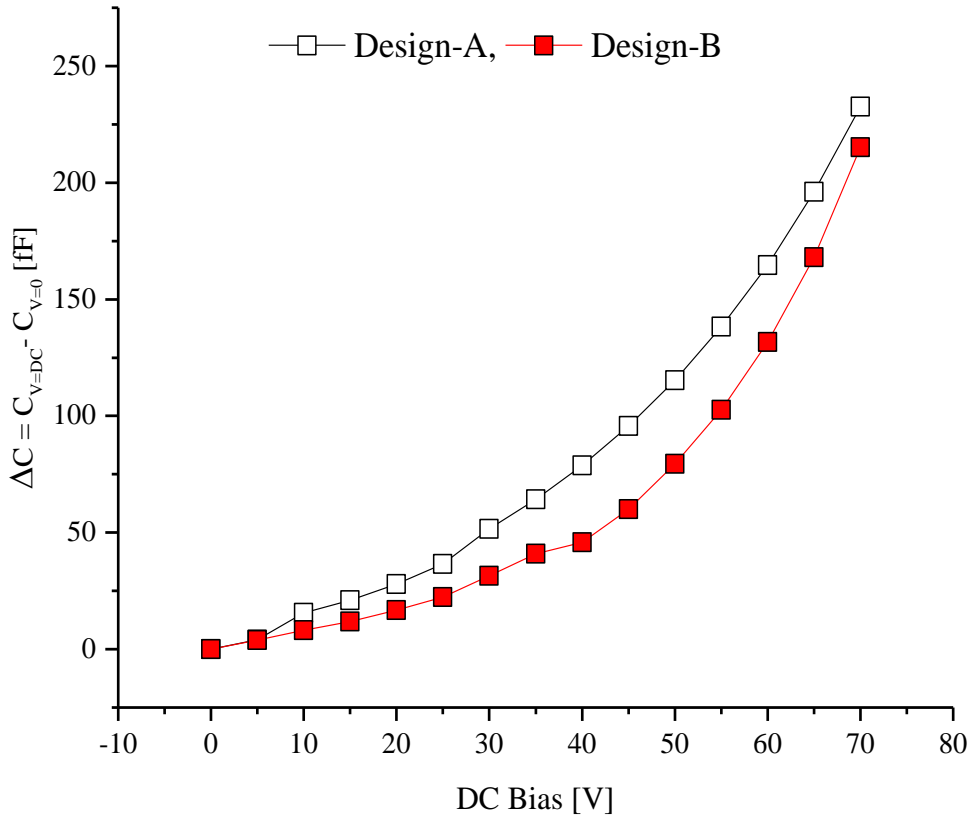
Figure 5.5. Differential capacitance of two 1-D arrays as a function of DC bias voltage. Each array consists of 22 single devices and each device has a membrane of 40 μm radius. A 50 mV, 5 MHz AC voltage was superimposed on the DC Bias.

In Figure 5.5, a slightly higher capacitance change is seen for Design-A array device (232 fF) than for Design-B array (215 fF). As mentioned earlier in Section 5.1.1, due to large parasitic elements in Design-A devices, a larger area and hence a larger capacitance was found in Design-A devices than that of Design-B. In addition, both devices showed increasing capacitance with increasing voltages which was a direct result of increasing membrane deflection (see Equation 3.3). The standard deviation, measured from averaging 801 measurement points for each signal, was found to be small ~0.89 fF.

The capacitance change (Design-A and Design-B) as a function of the DC bias confirms the basic functionality of the CMUT devices. As expected, the array showed

a higher capacitance than a single device, as the capacitance is proportional to the total membrane area. Therefore, an array with numerous CMUT devices would produce an increased acoustic power.

5.1.3 Impedance Measurements

The electrical impedance is an important parameter to characterize these CMUT devices. This is a complex quantity which gives the real part and the imaginary part of the measured device. Electrical impedance measurements were performed using an Agilent 4294A Precision Impedance Analyzer. The impedance analyzer was used as the ac source and a Keithly 237 high voltage source was used as the DC source. The impedance of a 1-D array (Design-A) was measured while the DC bias was increased from 0 to 90 V. As the bias-T had a maximum 100 V DC voltage limit, a 90 V DC bias was used at maximum, which was still below the theoretical collapse voltage of that device (~129 V) (see Section 3.3). A 50 mV ac voltage signal was superimposed on the DC Bias to enable the impedance measurement. This array consisted of 22 single devices; each device had a membrane of 40 µm radius. The change in real and imaginary part of the measured impedance of the 1-D array (Design-A) is shown in Figure 5.6.
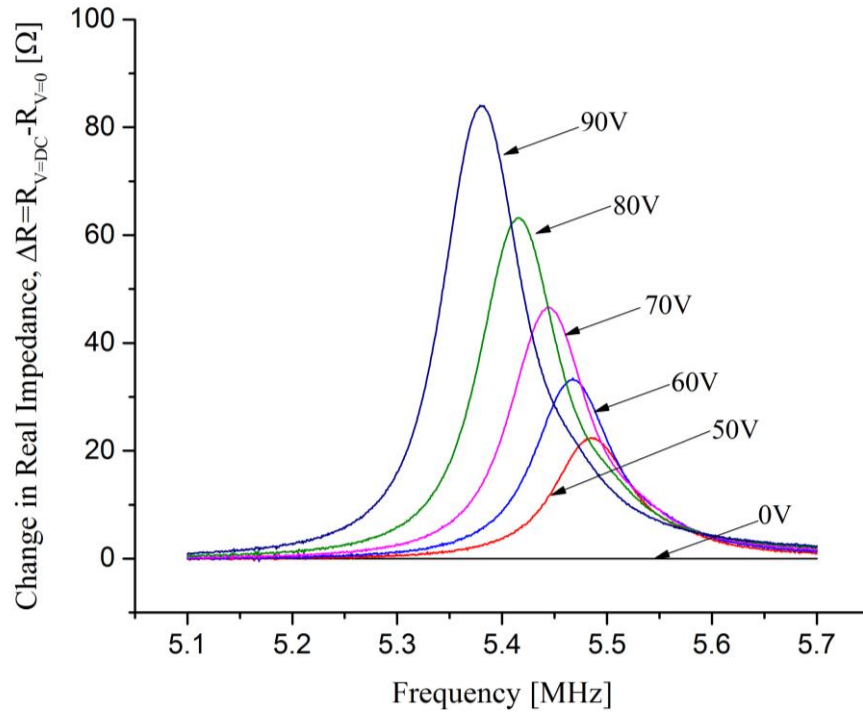
Figure 5.6. Change in real part of the impedance of a 1-D array (Design-A) as a function of frequency under various DC bias. A 50 mV AC voltage was superimposed on the DC Bias.

As the DC bias was increased, the change in the real part of the impedance (ΔR) also increased significantly. This change in the real impedance can be described by the following equivalent capacitor circuit model, shown in Figure 5.7.

From Figure 5.2, it was obvious that the CMUT devices had parasitic elements, which typically behave like series resistance (R_s), series inductance(L), and parallel resistance (R_p). The series resistance (R_s) and the series inductance(L) may arise from the wires and electrodes, whereas the parallel resistance (R_p) represents the loss of the dielectric material [54]. Typically, when the capacitance of a device is measured using an impedance measurement instrument, it is measured either in series mode, $C_s - R_s$ (a capacitor with a series resistance) or in parallel mode, $C_p - R_p$ (a capacitor with a parallel resistance). In this measurement, a series measurement circuit mode, $C_s - R_s$

was chosen, because this circuit mode allows the direct measurement of C, L, R values from the impedance characteristics. Therefore, a capacitor with parasitic elements can be represented as a $C - R - L$ circuit model as shown in Figure 5.7.
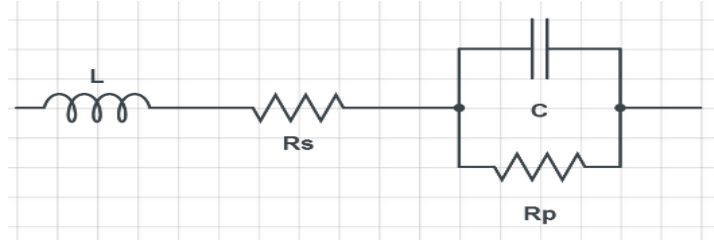
Figure 5.7. Schematic of a capacitor equivalent circuit model.

The impedance, Z of a typical $C - R - L$ circuit model can be written as [54]

$$Z = R_s + \frac{R_p}{1 + \omega^2 R_p{}^2 C^2} + \underbrace{j \frac{\omega L - \omega R_p{}^2 C + \omega^3 R_p{}^2 L C^2}{1 + \omega^2 R_p{}^2 C^2}}_{\text{Imaginary part}} \qquad 5.1$$

Real part

The parameters used in Equation 5.1 is listed in Table 5.1.

Table 5.1. Parameters used in a capacitor equivalent circuit model.

Z	Electrical impedance
R_s	Parasitic series resistance
R_p	Parasitic parallel resistance
C	Capacitance
L	Parasitic inductance
ω	Angular frequency

The real part of the impedance in Equation 5.1 is not only just a resistance, R_s but also a function of capacitance, C. When the DC bias is increased, the membrane deflection increases, as a result the capacitance increases and the real part of the

impedance changes, as shown in Equation 5.1. This in turn explains that the change in the real part of the impedance is due to the change in the membrane deflection with DC bias.

The real part of the impedance change, resulting from the membrane deflection, can be related with the total acoustic pressure. In Section 3.7.1, it was shown analytically that the larger membrane deflection causes a greater acoustic pressure. The expression for acoustic pressure is shown here for simplicity. If a CMUT membrane vibrates with a velocity $v = x * e^{jwt}$, the total acoustic pressure generated by that CMUT source at the far field ($r \gg R$) is given using Equation 3.63 [48].

$$p(r,\theta,t) = j\frac{\rho c x}{2} k R \times \frac{R}{r} \times e^{j(\omega t - k r)} \left[\frac{2 J_1 (kR \sin \theta)}{kR \sin \theta}\right],$$

Where p is the total acoustic pressure, v is the membrane velocity, x is the membrane deflection, ρ is the membrane density, k is the wave number, R is the membrane radius, c is the speed of sound, and r is the axial distance.

From Equation 3.63, the acoustic pressure of a vibrating CMUT device is shown to be directly proportional to the membrane deflection. Therefore, the significant real impedance change of the CMUT devices, resulting from the increased membrane deflection with DC bias, results an increased acoustic power.

Moreover, the transducer's behaviour over a wider frequency range can be investigated from Figure 5.6. It was observed that a CMUT offered a large change in the real impedance at or close to the resonant frequency which suggests a better performance at the resonant frequency in terms of acoustic power.

The impedance measurement was also conducted on the Design-B CMUT array to compare the performance with that of Design-A using the same experimental setup. The value of the real impedance was found to be maximum at the resonant frequency and that value was determined using the real impedance plot for both Design-A and Design-B devices. The maximum real impedances as a function of DC bias for both designs are shown in Figure 5.8.
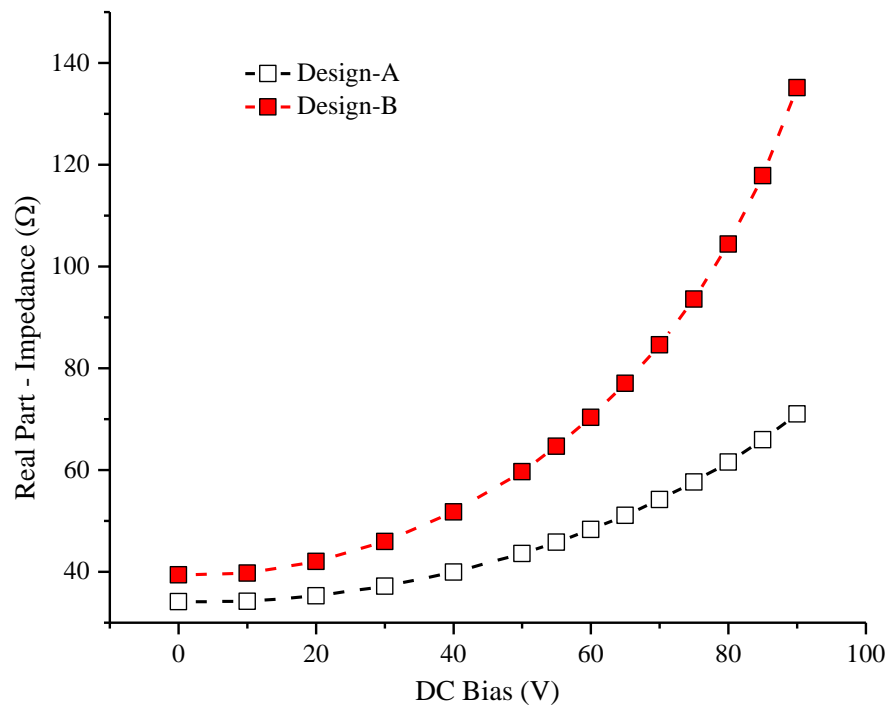
Figure 5.8. Maximum real part of impedance as a function of DC bias of two 1-D arrays (Design-A and Design-B). Each array consists of 22 devices and each device had a membrane of 40 μm radius.

It can be seen in Figure 5.8 that Design-B devices show a noticeably higher real part of impedance than that of Design-A. As mentioned in this section, the higher membrane deflection results a higher real part of impedance. Hence, Design-B membranes experienced a higher deflection than that of Design-A.

In addition, Design-A had a nitride layer between two electrodes that was shown previously in Figure 5.1. This nitride layer introduces an additional series capacitance along with the membrane capacitance. Therefore, at a given bias, some of the voltage is dropped across the nitride layer, reducing the electric field, and hence reducing the force on the membrane. For Design-B, that does not have the nitride layer, the field, and therefore the force is greater. As such, for a given bias, the membrane of Design-B deflects more than that of Design-A and thus produces more power.

Due to the absence of an additional series capacitance (as discussed in Section 5.1.2), Design-B devices show higher capacitance for a given bias, as a result higher real part of impedance and therefore higher acoustic power. Based on the measurements performed on Design-A and Design-B devices, the Design-B transducer would produce a higher acoustic power, at a given voltage, than would Design-A.

It was also found that when the applied voltage exceeded a certain voltage known as the "collapse voltage" (see Section 3.3), the membrane of Design-B collapsed on the bottom electrode and it was a non-reversible operation. In contrast, Design-A CMUTs could withstand a higher electric field and returned to its resting position after lowering the applied voltage. The voltage range for safe and proper transducer operation was investigated and is discussed in the next section.

5.1.4 Collapse Voltage Measurement

As mentioned in Section 3.3, when the electrostatic force is greater than the opposing membrane restoring force, the device becomes unstable. The membrane deflection increases continuously untill it touches the bottom electrode, as the opposing

force is lower than the electrostatic force. It was derived in Equation 3.13 and 3.14, for voltages greater than the collapse voltage, the membrane deflects more than one third of the gap height and as a result the membrane collapses onto the substrate. Typically, at the collapse voltage, the resonance of the membrane becomes unstable. The measurement of the resonant frequency, whether through the impedance or capacitance measurements, will show a sudden change in the shape of the curve close to the resonance. Therefore, it is cruicial to determine the collapse voltage, since operating biases below that point will allow for safe and proper operation of the transducer. For the collapse voltage measurement, the voltage between the membrane and the substrate was increased untill this istability was noticed through a sudden change in the shape of the resonance curve.
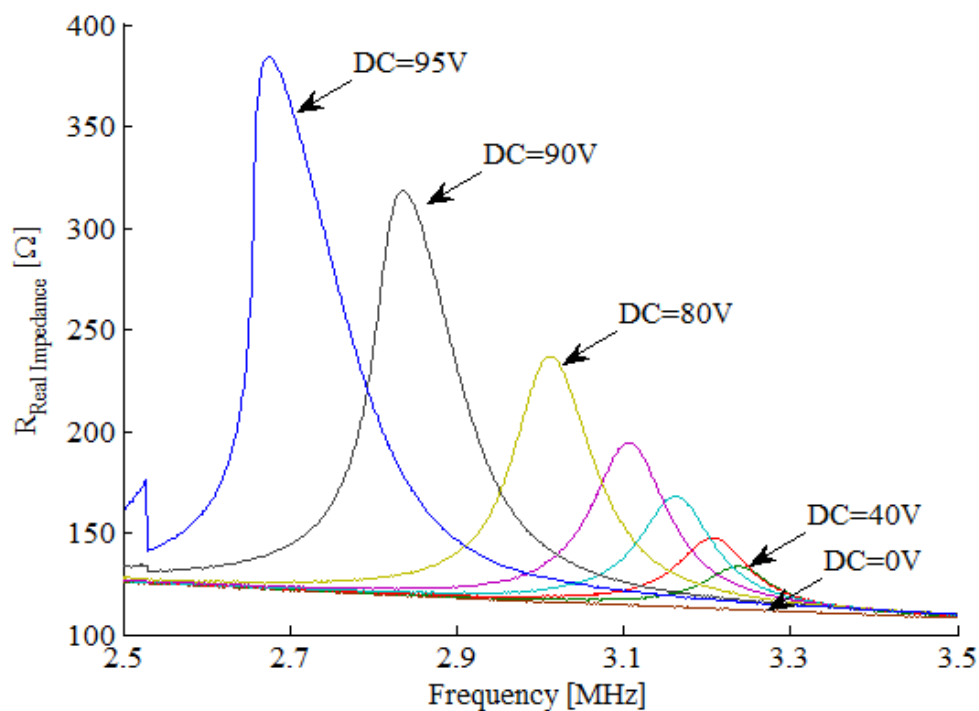
Figure 5.9. Collapse voltage measurement from a real impedance plot of a 50 μm radius membrane.

As the DC bias was increased, the resonance peak shifted to lower frequencies due to the spring softening effect (see Section 3.5). At about 90 V, an abrupt shift in the resonance curve is observed in Figure 5.9 which means that the CMUT membrane (50 µm radius) is approaching the collapse point. If a membrane is driven close to its collapse point, the frequency response becomes asymmetric, giving a low Q factor.

The collapse voltage of a CMUT device with 60 µm radius was also measured and found to be 65 V. Collapse voltage of other devices, with radius < 50 µm, were not determined using this method as their collapse voltages were greater than the highest DC voltage limit supported by the bias-T.

5.1.5 Spring Softening Effect

When a DC bias applied on a CMUT membrane is increased, the electrostatic force pulls the top membrane closer to the bottom electrode. As the membranes get closer to the bottom electrode, the electrostatic force increases further. This greater electrostatic force causes the membrane to vibrate more in downward direction. Due to this nonlinear increase in the electrostatic force, the membrane spring constant decreases and the resonant frequency shifts to lower value. This phenomenon is known as the "spring softening effect".

It was shown previously in Figure 3.4 that the resonant frequency shifts to lower value because of the decreased spring softening coefficient which is a result of increased membrane deflection. To investigate this spring softening phenomenon, the applied DC bias was increased from 0V to 90V with a 5V step size. The resonant

frequency shift of two 1-D arrays (Design-A and Design-B) as a function of DC bias is illustrated in Figure 5.10.
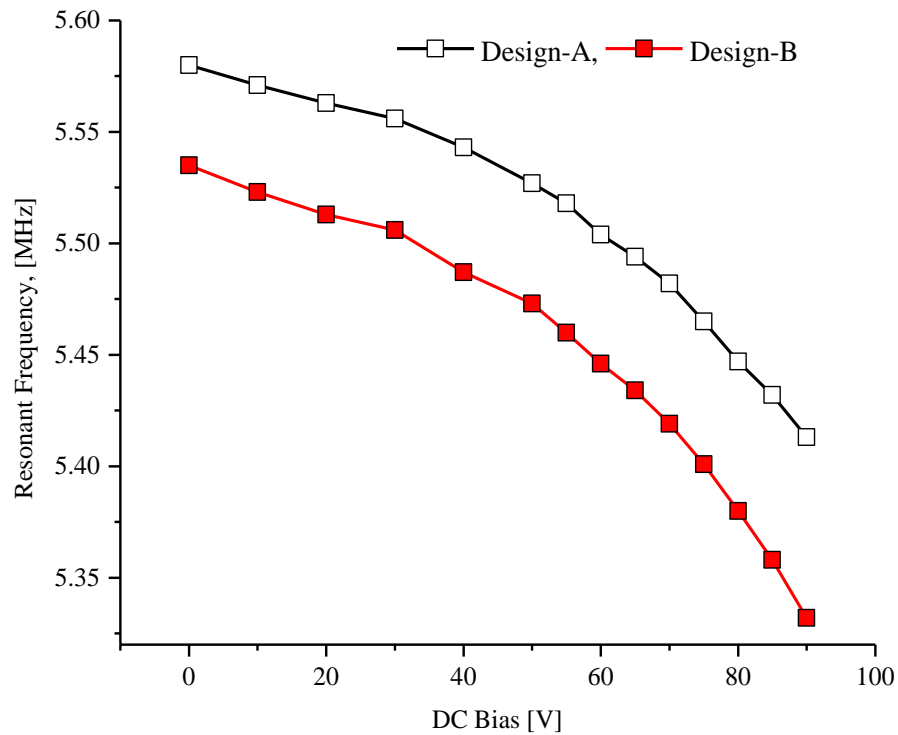
Figure 5.10. The resonant frequency shift of Design-A and Design-B 1-D CMUT arrays as a function of DC bias. A 50 mV AC voltage was superimposed on the DC bias.

The resonant frequency was extracted at the maximum real part of impedance from the real impedance plot in Figure 5.6. Both Design-A and Design-B transducers showed a quadratic frequency shift to lower values with increasing voltage, which agrees with the theoretical spring softening phenomenon.

The resonant frequency shift for Design-A (157 kHz at 90V) was found to be less than that for Design-B (192 kHz at 90V). As shown in Equation 3.44, the resonant frequency shifts linearly with the spring softening coefficient. As such, the larger frequency shift occurs due to the greater membrane deflection. Therefore, the Design-B transducers exhibited a larger frequency shift as a result of their greater membrane deflection relative to Design-A.

5.2 Optical Characterization

The optical characterization of CMUT devices designed by the author and described in this work, was performed by Arezoo Emadi (a post-doctoral fellow, University of Manitoba), using a Polytec Micro System Analyzer (MSA-500) at the University of British Columbia. In this system, a laser Doppler vibrometer (LDV) measures the surface vibration of an object by detecting the Doppler shift of a laser. When a wave is reflected from a moving surface, the frequency of the wave shifts, which is known as the Doppler effect and the shift may be expressed as

$$f_D = 2 * \frac{\text{velocity of the surface}}{\text{wavelength}} \qquad 5.2$$

The velocity of a vibrating membrane can be found by the Doppler shift and the frequency at which the membrane is operating. Different structural vibration modes of a CMUT membrane can also be visualized using a microscope integrated with the laser Doppler vibrometer.

5.2.1 Surface Deflection Measurement

The experimental setup for optical characterization is shown in Figure 5.11. The micro system analyzer (MSA) unit consisted of a data management system, a junction box, a vibrometer that provides a laser source and a vibrometer controller. The displacement of the CMUT devices was measured with a 1 V ac voltage signal superimposed on 9 V DC bias and the frequency was swept from 0-20 MHz with a 3.1 kHz step size.
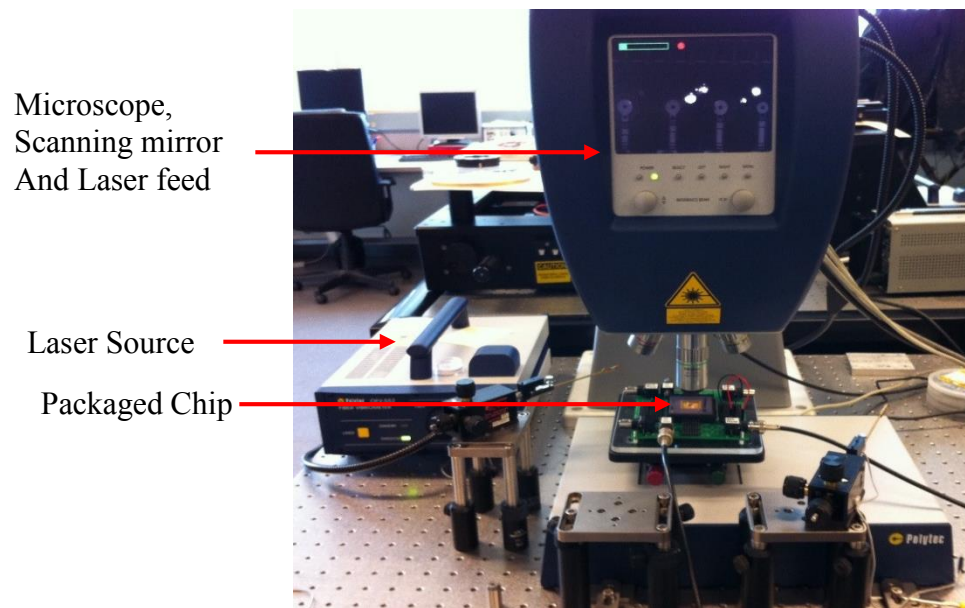
Figure 5.11. Front view of the experimental set-up showing a packaged chip, laser source, microscope, scanning mirror, and laser feed.
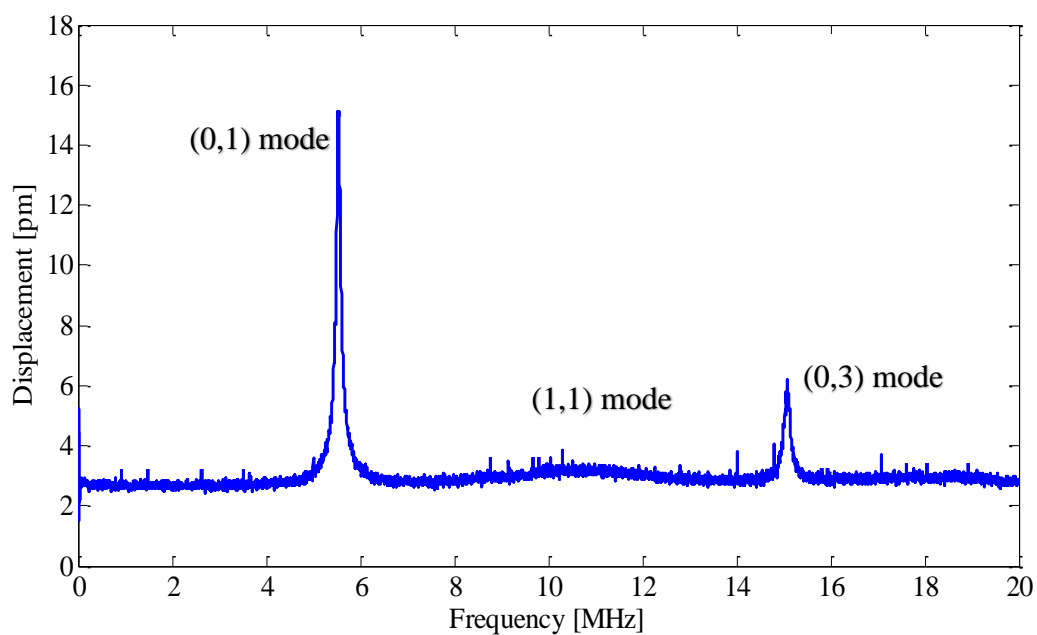
Figure 5.12. Frequency response of a single CMUT with 40 µm membrane radius. A 1V AC voltage is superimposed on 9V DC bias.

The displacement profile obtained from the vibrometer measurement of a 40 µm membrane radius is shown as a function of frequency in Figure 5.12. There are three vibration modes shown in the data where the fundamental (0,1) resonant mode

occurred at 5.5 MHz at which a higher deflection was observed. The membrane in the fundamental mode vibrates like a monopole source and emits the sound wave most efficiently. The (1,1) mode at 10.68 MHz and the (0,3) mode at 15.02 MHz can also be seen in the figure, where the deflection is much smaller than the fundamental (0,1) mode. The displacement profiles of other single devices and 1-D arrays were also measured using the same experimental setup.

The resonant frequencies of single devices and 1-D arrays were determined using the surface displacement profile (see Figure 5.12), when the membrane displacement was at its maximum. The resonant frequencies were also extracted from the electrical measurement data using the real impedance plot (see Section 5.1.3 and Figure 5.6). The resonant frequency using the laser Doppler vibrometer (LDV) was compared with that from the electrical measurement and was found to be in good agreement, which is shown in Figure 5.13.
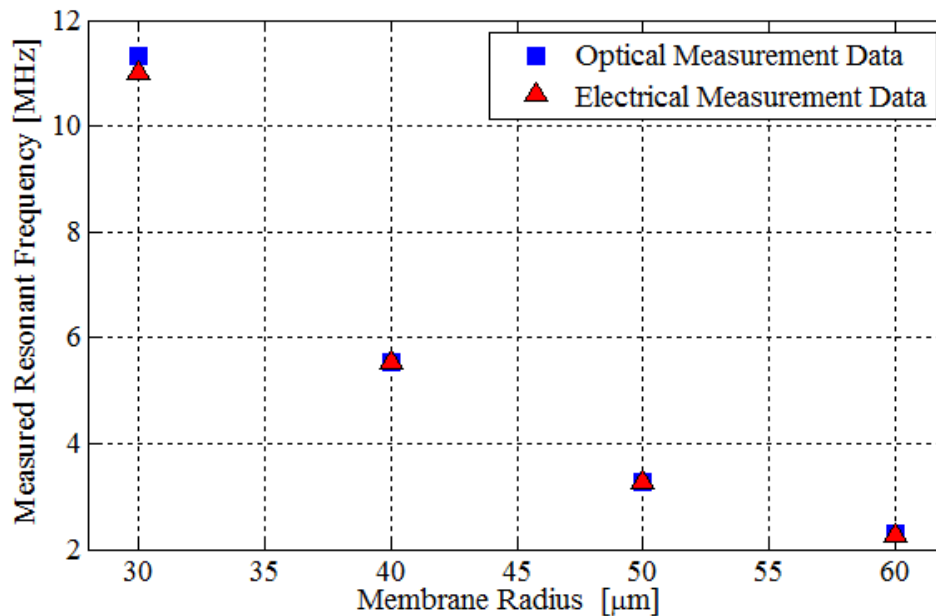
Figure 5.13. Comparison between the optically measured and electrically measured resonant frequencies of different sizes CMUT devices.

5.2.2 Vibration Modes and Resonant Frequency

The Micro System Analyzer provides a 3-D visualization of structural vibrations using the integrated microscope. For visualization of different vibration modes, the CMUT devices were actuated with 9 V DC bias and a 1 V ac voltage signal was superimposed on it.

(a)   (b)

(c)
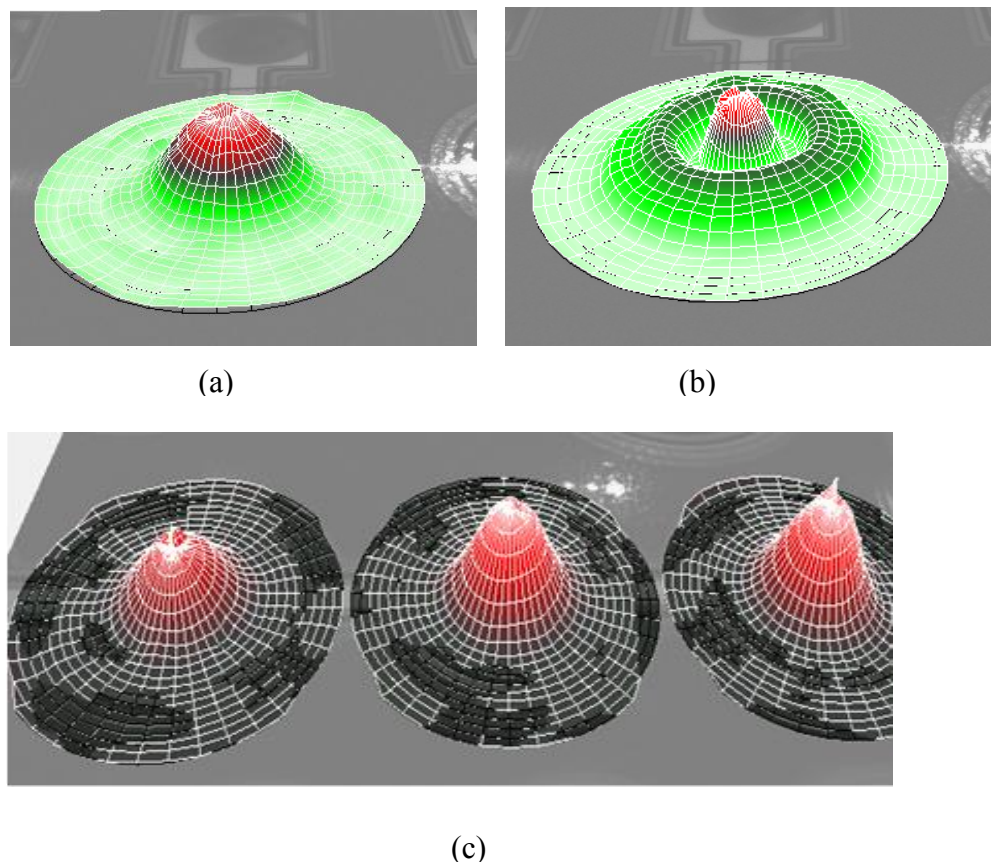
Figure 5.14. (a) (0,1) mode vibrating at 3.284 MHz (b) (0,3) mode vibrating at 10.684 MHz of a single device (Design-B) with 50 µm membrane radius and (c) (0,1) mode vibrating at 15.52 MHz of a 1-D array (Design-A) with 22 membranes, with each membrane 40 µm radius (a small portion of the array is shown here).

The vibration profile of a single device (50 µm radius, Design-B) is shown in Figure 5.14 (a) and (b), where the (0,1) mode vibrating at 3.28 MHz and the (0,3) mode vibrating at 10.684 MHz can be seen. The (0,1) vibration mode a 1-D array (40 µm membrane radius, Design-A) is also shown in Figure 5.14 (c). It can be seen from Figure

5.14 that the CMUT device, operating at its fundamental (0,1) resonant mode, behaves like a monopole source, would offer significantly higher displacement (Figure 5.12) and therefore would produce a higher acoustic pressure.

Chapter 6: Acoustic Characterization of CMUTs

In order to demonstrate the capability of a CMUT device to produce an acoustic pressure wave in response to an electrical signal, two sets of acoustic experiments were performed. In those experiments, the fabricated CMUT device was used as the transmitter and a commercial air transducer was used as the receiver. The measured acoustic signals were analyzed and are shown and discussed in this chapter.

6.1 Pitch-Catch Acoustic Experiment Setup

A "pitch-catch" measurement was performed for the acoustic characterization of the CMUT devices. In a "pitch-catch" measurement, one device "pitches" (transmits) and a second device "catches" (receives). In this experiment, a CMUT array (Design-A) was used as the transmitter and a Microacoustics[TM] BAT-1 (Broadband Air-coupled Transducer-1) air transducer was used as the receiver. This experiment was performed in the department of Physics and Astronomy at the University of Manitoba. The CMUT array was made of 22 circular membranes; each membrane had a radius of 40 µm. The array was operated at various bias ranging from 65-90 V. Two different types of ac voltage signals, burst and pulse, which will be explained later, were superimposed on the DC bias. A custom designed bias-T was used to mix the DC and ac voltages and that were then applied to the CMUT. A block diagram, showing the transmitter and the detector biasing configuration, is shown in Figure 6.1.

The CMUT, which was on a test fixture, was mounted on a XYZ positioner and the detector was positioned on a linear motion stage. The BAT detector was biased using a trans-impedance preamplifier Q-Amp[TM]. The experimental setup, shown in

Figure 6.2, illustrates the side view of the detector, and the CMUT transmitter in a test fixture. The signal, detected by the BAT transducer, was amplified using a preamplifier and then recorded with a high speed oscilloscope.
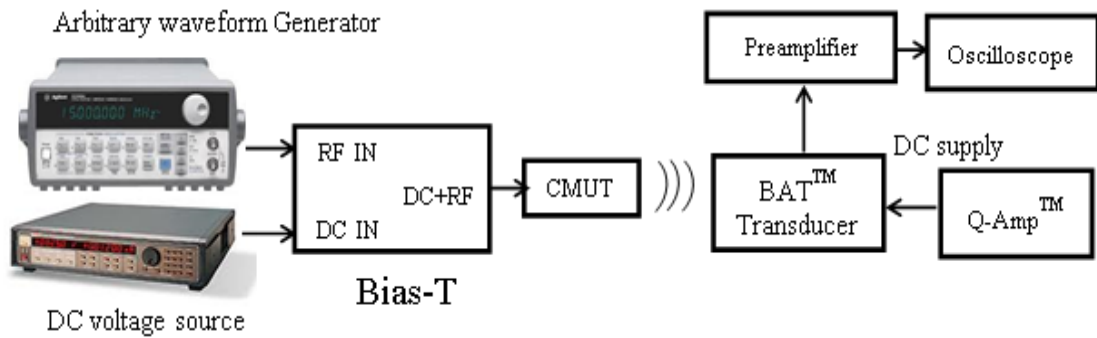
Figure 6.1. Block diagram of the transmitter and the receiver biasing configuration.
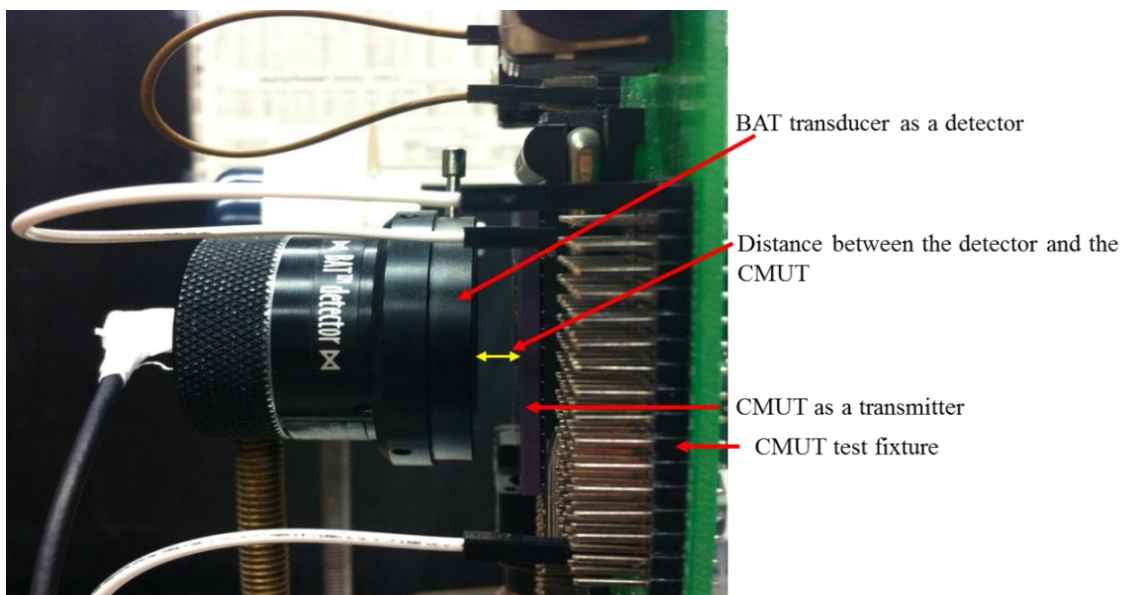
Figure 6.2. The side view of the experimental setup showing the detector and the CMUT transmitter.

6.1.1 Burst Signal Excitation

In the burst signal transmission measurement, the CMUT array was biased with a DC voltage at 65 V, 75 V, and 85 V respectively using a Keithly 237 high voltage

source. A 5 cycle 10 V_{p-p} sinusoidal burst signal at 1MHz was applied on top of the DC

bias using an Agilent 33120A Signal generator. The mixed DC/ac burst signal was then

applied to the CMUT. The burst repetition frequency was 1 kHz. The detector

bandwidth was between 40 kHz and 2.25 MHz.

The CMUT device generated an acoustic signal in response to an applied

electrical signal and transmitted that signal into the air. The receiver, which was

positioned at ~9 mm in front of the CMUT, detected the generated acoustic signal and

is shown in Figure 6.3. The CMUT was operated at V_{DC}=85 V and V_{AC}=10 V_{p-p} at 1

MHz.
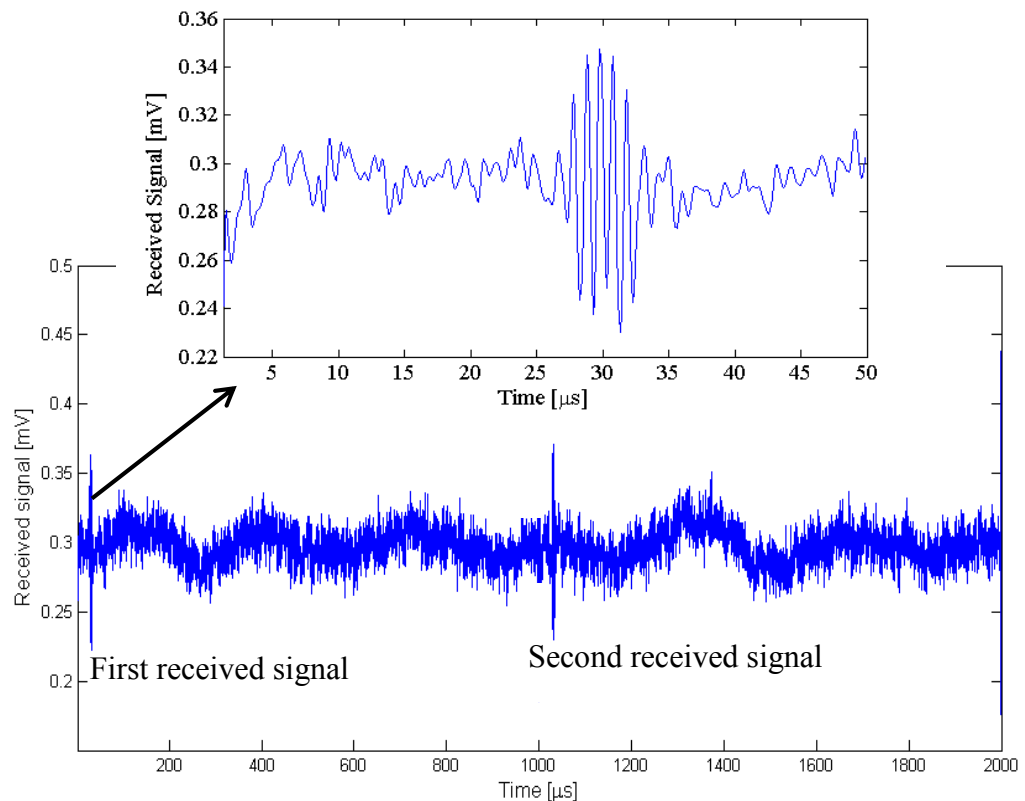
Figure 6.3. The signal received by the BAT-1 air transducer in response to a 10 V_{p-p}, 5 cycle sinusoidal burst signal with a 85 V DC bias applied to the CMUT. The CMUT consisted of 22 devices with each having 40 μm radius membrane. The enlargement of the first received signal is shown inset.

The time delay between the input burst signal being applied to the CMUT device and the first received signal was found to be ~26.5 µs. Using the speed of sound as 343 m/s [55] and the measured propagation time (~26.5 µs) of the generated ultrasound, the separation between the CMUT and the detector was found to be ~9.08 mm, which is close to the actual distance (~9 mm). The second signal was received at ~1028 µs which also agrees with the distance with 1 KHz burst repetition frequency. The experimental results demonstrated that the fabricated CMUTs can successfully produce acoustic signals in response to a burst signal.

However, it is also important to investigate the CMUT's capability to produce an acoustic signal using a lower voltage pulse excitation. In the next section, a "pitch-catch" measurement using a pulse excitation is described and discussed.

6.1.2 Pulse Excitation

In the pulse transmission measurement, the same CMUT device that was used for the burst measurement was biased at 90 V. A 500 ns, 10 V unipolar pulse with 1 kHz pulse repetition frequency was applied using a TGA 1244 Arbitrary waveform generator. The pulse excited the membrane and produced an acoustic signal which was then measured by the BAT transducer and is shown in Figure 6.4.
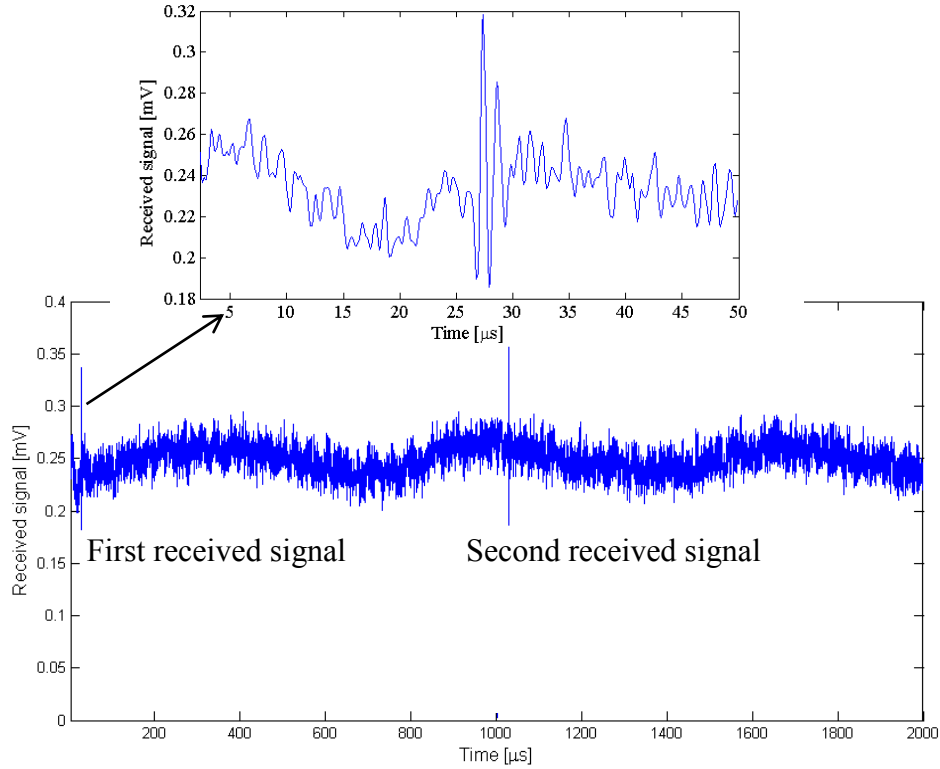
Figure 6.4. The output acoustic signal received by the BAT-1 transducer when a 500 ns, 10 V unipolar pulse on V_{DC} = 90 V was applied to the CMUT. The enlargement of the first received signal is shown inset.

The propagation time of the acoustic signal was found to be ~26.5 μs. The propagation time (~26.5 μs) and the separation distance (~9 mm) corresponds to the speed of sound as 339 m/s which is close to the typical speed of sound at room temperature (343 m/s) [55].

The received signal has significant background noise. Due to the impedance mismatch between the CMUT and air, a substantial portion of the signal is reflected. Acoustic impedance mismatch means a difference in acoustic impedances between two mediums which causes a significant signal loss at the interface. However, this experiment still successfully verified that even in a pulse mode, the CMUTs response can be measured.

6.2 Attenuation of the Received Signal:

Attenuation refers to a loss of a signal amplitude through a medium over a distance. In most cases, the attenuation is caused in the form of scattering and absorption. Scattering of a wave happens when colliding with some objects and the wave is redistributed in all directions. Absorption refers to the sound wave being absorbed by any object or by air. In order to investigate the attenuation of the generated acoustic signal with distance, the air transducer mounted on a linear motion stage was moved manually from the CMUT. The applied bias to the CMUT was 85 V DC with a 5 cycle 10 V_{p-p} sinusoidal burst signal at 1MHz. The detected acoustic signals as a function of the axial distance is shown in Figure 6.5.
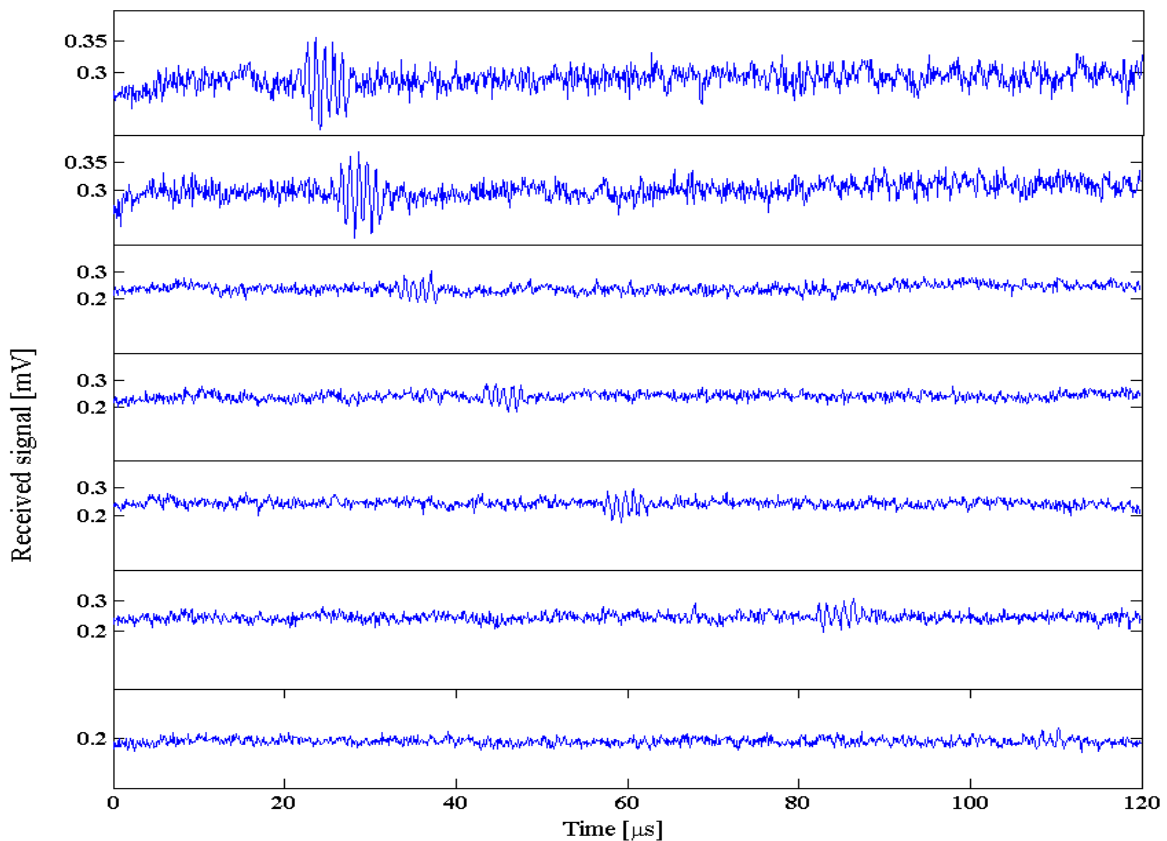
Figure 6.5. The reduction of the received signal amplitude with distance, of a CMUT array biased at V_{DC}=85 V and V_{AC}=10 V_{p-p}.

As expected, the signal amplitude dropped with increasing distance, shown in Figure 6.5. The attenuation of the received signal was likely substantially due to the acoustic impedance mismatch between the air and the CMUT membrane. In ultrasonic imaging, the acoustic impedance of the transmitter and the outside medium ideally should be perfectly matched in order to minimize the signal reflection. The impedance of the CMUT devices, reported by Ergun et al. [10], which was ~1.5 ([Kg/(m^2.s)]*10^6), was found to be much higher than the air impedance (0.0004 [Kg/(m^2.s)]*10^6). The impedance of air can be found by the product of the density of air and the speed of sound.

The acoustic signals were measured for various combinations of DC and ac voltages. A 5 cycle sinusoidal burst signal at 1 MHz was applied with the DC bias. The received signals under these bias conditions are illustrated in Figure 6.6. Each data point in Figure 6.6 represents an average peak to peak signal, obtained from averaging all the peaks of each signal data. The error bar of each signal was calculated by taking into account the difference between the peak and the average data of each signal. It can be seen that the signal amplitude significantly increases with an increased ac voltage; while the signal amplitude also increases with increasing DC bias, but the effect appears less than that with increasing ac signal. The data shown in Figure 6.6 can be verified by the theoretical dynamic behavior of a CMUT model (see Section 3.4) which is repeated here for the reader's convenience.

$$V(t) = V_{DC} + V_{AC} \sin \omega t$$

$$F_{DC+AC} = \frac{\varepsilon A V(t)^2}{2(d_0 - x)^2}$$

$$= \frac{\varepsilon A}{2(d_0 - x)^2} \left[(V_{DC}^2 + \frac{1}{2} V_{AC}^2) + 2 V_{DC} V_{AC} \sin \omega t - \frac{1}{2} V_{AC}^2 \cos 2\omega t \right]$$

When, $V_{AC} \ll V_{DC}$

$$F_{DC+AC} \approx \frac{\varepsilon A}{2(d_0 - x)^2} V_{DC}{}^2 + \frac{\varepsilon A V_{DC}}{(d_0 - x)^2} V_{AC}$$

6.1

where F_{DC+AC} is the total force acting on the membrane due to applied ac and DC bias, ε is the dielectric permittivity of free space, A is the membrane area, $V_{(t)}$ is the total voltage applied, d_0 is the initial gap height and x is the vertical membrane displacement under an applied bias.
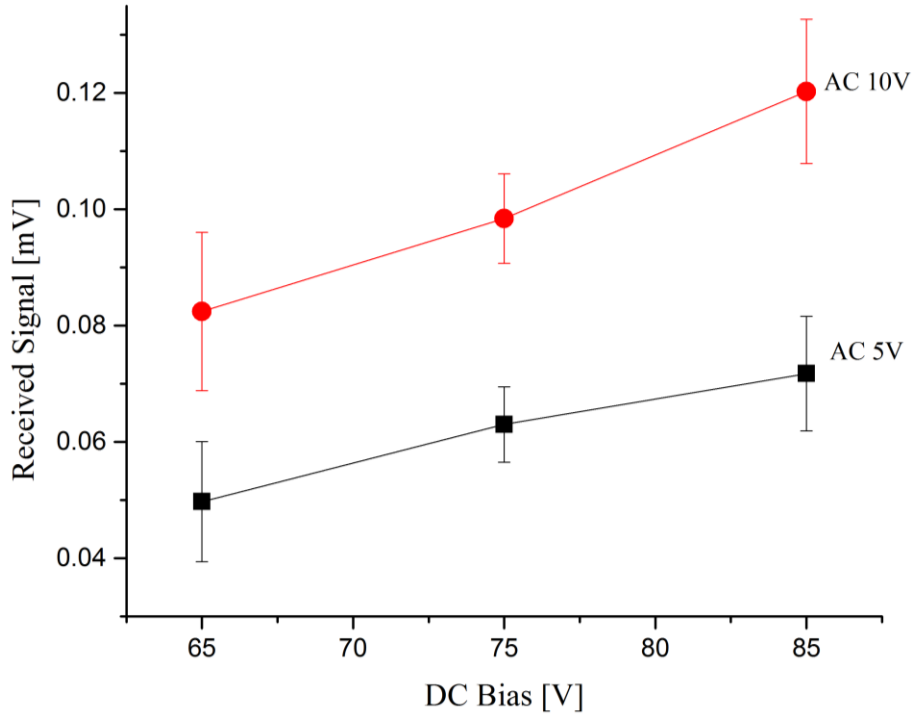
Figure 6.6. The received signal amplitude as a function of various DC biases with V_{AC}=5 V and V_{AC}=10 V.

From Equation 6.1, an applied DC bias increases the device sensitivity by pulling the membrane toward the substrate and an ac signal causes the vibration of the membrane and produces an acoustic wave. This theoretical dynamic behavior is clearly

86

observed in the experimental data, shown in Figure 6.6, where the higher vibration amplitude was the result of the higher ac voltages.

Conventionally the CMUT devices are operated at or close to the resonant frequency to get maximum deflection, which in turn produces maximum acoustic power. The CMUTs were operated at a frequency (1 MHz) which was far from the device resonant frequency (5.5 MHz). Even though the CMUT was operated well below its resonant frequency, it still produced a sufficient acoustic signal that could be detected. The maximum applied DC bias (85 V) was also well below the theoretical collapse voltage (~129 V) of that device. The signal intensity would increase substantially if the CMUTs were biased closer to the collapse voltage.

6.3 Attenuation Coefficient Measurement

Attenuation is an important parameter in ultrasound applications as it determines the amount of signal amplitude reduction with distance. The decay of acoustic signal intensity with distance can be expressed, in its simplest form, by the equation [52]

$$I_x = I_0 e^{-\alpha x}, \qquad\qquad 6.2$$

where x is the propagation distance, I is the signal amplitude propagate at position x distance, I_0 is the initial signal amplitude at the source, $x = 0$, α is the attenuation coefficient of the medium.

The attenuation coefficient in a particular medium at room temperature can be calculated using the Stokes law and is given by [52]

$$\alpha = \frac{\omega^2 \eta}{2\rho c^3},$$

6.3

where $\omega = 2\pi f$ is the angular frequency, η is the dynamic viscosity, ρ is the density of the medium, and c is the speed of sound in that medium. Typically the attenuation coefficient is measured in m^{-1}.

Acoustic signals were also measured at different distances using the BAT-1 transducer and the experimental set-up described in Section 6.1. The measured peak to peak signal intensity, I_x was then plotted as a function of distance x (see Figure 6.7). The error bar of each signal was found by the difference between the peak and the average data of each signal.
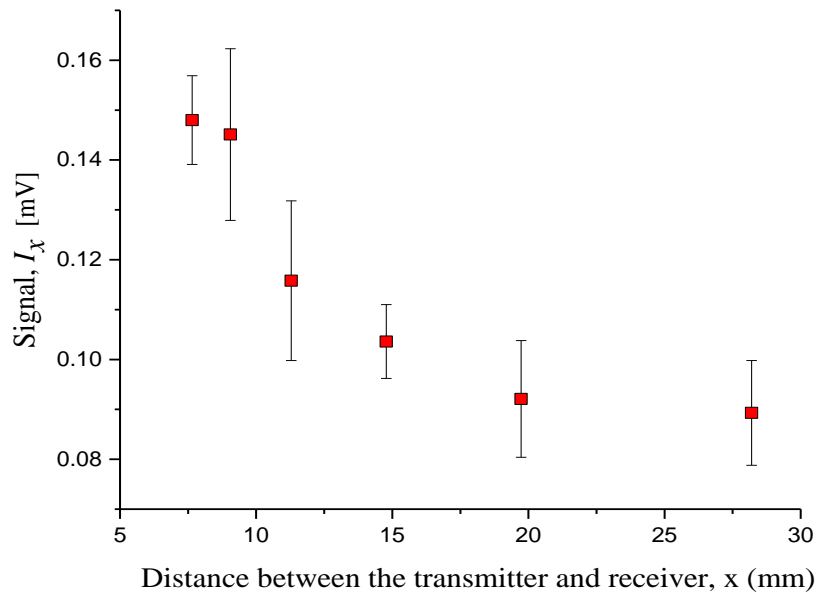
Figure 6.7. The measured peak to peak signal amplitude as a function of distance, while the transmitting CMUT was biased at V$_{DC}$=85V and V$_{AC}$=10V$_{p\text{-}p}$ burst signal at 1 MHz.

In order to determine the attenuation coefficient, from Figure 6.7, the logarithm of the received signal amplitude is plotted as a function of distance. A linear fitted curve was also plotted to find the slope of the data and to find the "goodness" of the data to the fitted line.
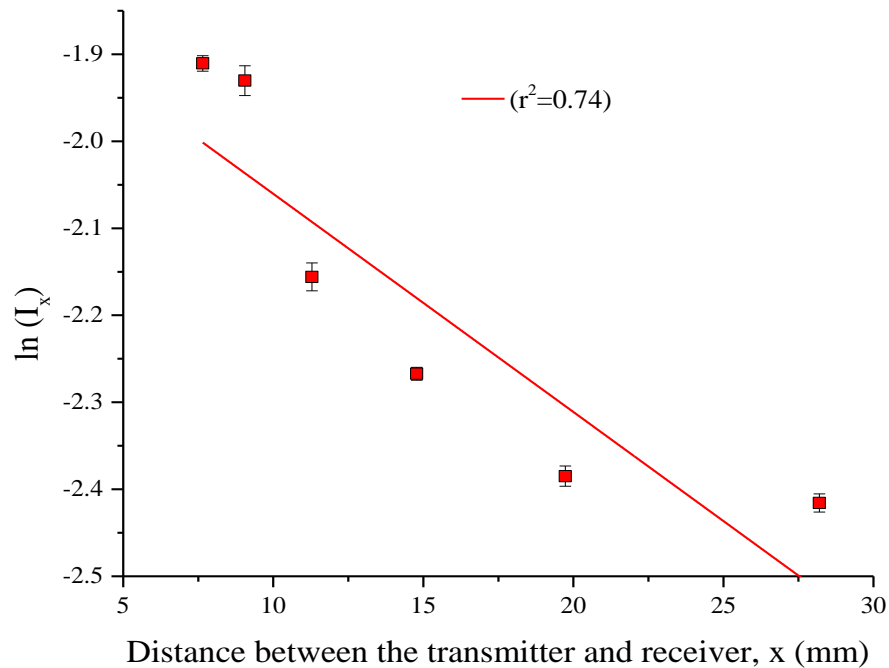
Figure 6.8. Logarithmic peak to peak signal amplitude decrease as a function of distance for a CMUT biased at 85 V DC and a 10 V_{p-p}, 5 cycle sinusoidal burst ac signal at 1 MHz was applied on it.

The correlation coefficient, r^2, is a statistical measure that tells how close the data are to the fitted line. The r^2 value was found to be 0.74 as shown in Figure 6.8. While the r^2 value for the data in Figure 6.8 is not good, the correlation coefficient for I_x as a function of x (Figure 6.7) was found to be even lower at 0.68. The slightly better fit from the log-linear plot using these data can be used to extract the attenuation coefficient, α.

The slope of $ln(I_x)$ (i.e. the rate of signal decay) gave a value of attenuation coefficient of 25 m^{-1}. The theoretical attenuation coefficient, using Stoke's law was calculated as ~9 m^{-1}. The parameter values [55], used for calculating attenuation coefficient using Equation 6.3, are listed in Table 6.1.

Table 6.1. Parameter used for theoretical attenuation coefficient calculation.

Symbol	Expression	Value
f	Frequency	1 MHz
η	Dynamic viscosity at room temperature, 20^0 C	~$1.81*10^{-5}$ kg/m.s [55]
ρ	Density of the medium	1.00 kg/m^3
c	Speed of sound	343 m/s
	Room temperature	20^0 C

This discrepancy between the extracted and the calculated value is still unknown. There are several possible explanations for this difference. These could include a slight misalignment of the detector's position, or angle which could be coupled into the uncertainty in the CMUTs beam directivity pattern (see Section 3.8.2).

While not explicitly measured, the temperature variations due to heat from the nearby equipment may also have an effect in signal detection. An increase in room temperature from 18^0 C to 25^0 C causes an increase of ~3.5% in the air viscosity [55]. The effect on the calculated attenuation coefficient, Equation 6.3, is an increase of ~19%, using the data from [55]. The air viscosity change and hence the attenuation coefficient change due to an increase in room temperature might be a significant contribution to the discrepancy between the value of the attenuation coefficient calculated from the slope of Figure 6.8 and that calculated from theory. A standard, room temperature of 20^0 C was assumed in all measurements and analysis.

Chapter 7 : Conclusions and Future Work

7.1 Conclusions

In this work, several single and 1-D array CMUT devices were designed based on the COMSOL finite element simulations and were fabricated using a PolyMUMPs fabrication technology. Electrical measurements were performed to demonstrate the basic functionality of those devices through capacitance and electrical impedance measurements. The measured capacitance and impedance were found to increase with increasing bias voltage, which was a direct result of increasing membrane deflection. The reduction of the effective gap height due to that increased membrane deflection caused an increase in the electrostatic force and the resultant force was found to soften the membrane stiffness. As a result of this spring softening effect, a decrease in the device resonant frequency was observed, which also indicates a larger membrane displacement and in turn enhances the transducer performance.

The collapse voltage of some of the devices was measured to establish the transducer's stable operating point. Electrical impedance measurements at various bias conditions were performed to discover this operating point.

Optical measurements were conducted to measure the deflection profiles of CMUT devices at different resonant frequency modes, using a Polytech Micro System Analyzer. The resonant frequency, measured using this optical measurement, was found to be in good agreement when compared with that derived from the electrical measurement.

Acoustic measurements were performed to demonstrate the capability of the CMUT to produce an acoustic signal. It was found that the CMUT produced a sufficient acoustic signal that could be detected, even though it was operated well below its resonant frequency. These experimental results confirm that this CMUT can potentially be used as an ultrasonic transducer.

7.2 Suggested Future Works

Although the experimental results demonstrated the transmission operation of the CMUTs, to implement the device as a "transducer", the receiving operation also needs to be investigated. In the receiving operation, an incoming ultrasound causes a membrane to vibrate, resulting a change in the device capacitance that could be detected through the measurement of a displacement current.

As the output power would scale with the number of devices, large CMUT arrays (1-D and 2-D) could also be fabricated and tested as increased output power should lead to an improved image quality for ultrasonic imaging applications.

References

[1]   T. L. Szabo, Diagnostic Ultrasound Imaging: Inside Out, San Diego: Elseview Academic Press, 2004.

[2]   Y. Honda, and P. J. Fitzgerald, "Frontiers in Intravascular Imaging Technologies," *Circulation,* vol. 117, pp. 2024-2037, 2008.

[3]   Ildstad, E., Sletbak, J., Faremo, H., "Water Treeing and Breakdown Strength Reduction of XPLE insulation," *Proceedings of the 3rd International Conference on Conduction and Breakdown in Solid Dielectrics,* pp. 494-499, Jul 1989.

[4]   T. Kumazawa and R. Tanihuchi, "Detection of weak radiation involving generation and progress of water tree," *Electr. Eng. Japan,* Vols. 164, No. 2, pp. 1-9, 2008.

[5]   G. Thomas, D. Flores-Tapia, S. Pistorius, N. Fernando, "Synthetic aperture ultrasound imaging of XLPE insulation of underground power cables," *IEEE Electrical Insulation Magazine,* Vols. 26, No. 34, pp. 24-34, 2010.

[6]   D. W. Auckland, A. J. McGrail, C. D. Smith, and B. R. Varlow., "The use of ultrasound for the detection of water trees in XLPE cable," *Int. Conf. Conduct. Breakdown Solid Dielectr.,* p. 681–684, 1995.

[7]   D. W. Auckland, A. J. McGrail, C. D. Smith, B. R. Varlow, J. Zhao,D. Zhu, "Application of ultrasound to the inspection of insulation," *IEEE proc. Meas. Technol. Sci.,,* vol. 143, pp. 177-181, May, 1996.

[8]   Matzuwa., K., "Capacitive Ultrasonic Transducer," *Phys. Soc. Jap.,* vol. 13, p. 1533, 1958.

[9]   W. Kuhl, G. R. Schodder, and F. K. Schodder,, "Condenser transmitters and microphones with solid dielectric for airborne ultrasonics," *Acoustica,* vol. 4, pp. 520-532, 1954.

[10]   Ergun, Arif S., Yaralioglu, Goksen G., and Khuri-Yakub, Butrus T., " Capacitive Micromachined Ultrasonic Transducers: Theory and Technology," *Areospace Engineering,* vol. 16(2), pp. 76-84, April 2003.

[11]   J. H. Cantrell and J. S. Heyman, "Broadband electrostatic acoustic transducer for ultrasonic measurements in liquid," *Rev. Sci. Instrum.,* vol. 50, pp. 31-33, Jan. 1979.

[12]   B.T. Khuri-Yakub, O. Oralkon, M. Kupnic, "Next-gen ultrasound," *IEEE Spectrum46,* pp. 44-54, 2009.

[13]   M. I. Haller and B. T. Khuri-Yakub, "A surface micromachined electrostatic ultrasonic air transducer," *IEEE Ultrason. Symp.,,* pp. 1241-1244, 1994.

[14]   Torndahl, M.; Almqvist, M.; Wallman, Lars; Persson, H.W.; Lindstrom, K., "Characterisation and comparison of a cMUT versus a piezoelectric transducer for air applications," *IEEE Ultrasonics Symposium,* vol. 2, pp. 1023-1026, Oct 2002.

[15]   D. M. Mills, "Medical Imaging with Capacitive Micromachined Ultrasound Transducer (cMUT) Arrays," *IEEE Ultrasonics Symposium,* vol. 1, pp. 384-390, 2004.

[16]   Alessandro Caronti, G. Caliano, R. Carotenuto, A. Savoia, M. Pappalardo, E. Cianci, V. Foglietti, "Capacitive micromachined ultrasonic transducer (CMUT) arrays for medical imaging," *Microelectronics Journal,,* vol. 37, no. 8, pp. 770-777, August 2006.

[17]   December 2013. [Online]. Available: http://www.ndt-ed.org/GeneralResources/MaterialProperties/UT/ut_matlprop_liquids.htm.

[18]   Igal ladabaum, Xuechen Jin, Hyongsok T. Soh, Butrus T. Khuri-Yakub, "Surface Micromachined capacitive ultrasonic transducers," in *IEEE Transactions on Ultrasonics, Ferroelectrics, and Frequency Control*, 1998.

[19]   H. T. Soh, I. Ladabaum, A. Atalar, C. F. Quate, and B. T. Khuri- Yakub, "Silicon icromachined ultrasonic immersion transducers," *Appl. Phys. Lett.,* vol. 69, pp. 3674-3676, 1996.

[20] X Zhuang, A Nikoozadeh, M A Beasley, G G Yaralioglue, "Biocompatible coatings for CMUTs in a harsh, aqueous environment," *Micromechanics and Microengineering,* vol. 17, pp. 994-1001, 2007.

[21] T. A. Emadi, and D. A. Buchanan , "Multiple moving membrane CMUT with enlarged membrane displacement and low pull-down voltage," in *IEEE Electron Device Letters*, 2013.

[22] Ergun AS, Huang Y, Zhuang X, Oralkan O, Yaralioglu GG, Khuri-Yakub BT, "Capacitive micromachined ultrasonic transducers: fabrication technology," *IEEE Trans Ultrason Ferroelectr Freq Control. 2005 Dec;52(12):2242-58.,* vol. 52, no. 12, pp. 2242-58, Dec 2005.

[23] Oralkan Ö, Ergun S, Johnson JA, Karaman M, Demirci U, Kaviani K, Lee TH, and Khuri-Yakub BT, "Capacitive Micromachined Ultrasonic Transducers: Next Generation Arrays for Acoustic Imaging?," *IEEE Transactions on Ultrasonics, Ferroelectrics and Frequency Control,* vol. 49, pp. 1596-1610, 2002.

[24] Akash Jain, David W, Greve, and Irving J. Oppenheim, "Experiments in Ultrasonic flaw detection using a MEMS transducer," *Smart Structures and Materials 2003: Smart Systems and Nondestructive Evaluation for Civil Infrastructures,* pp. 431-439, 2003.

[25] "www.hitachi-medical.co.jp/medix/pdf/vol51/P31-34.pdf," December 2013. [Online].

[26] M. I. Haller and B. T. Khuri-Yakub, "A surface micromachined electrostatic ultrasonic air transducer," *IEEE Transactions on Ultrasonics, Ferroelectrics and Frequency Control,* Vols. 43, No. 1, pp. 1-6, 1996.

[27] Jin Xuecheng, Ladabaum I, Khuri-Yakub B T, "The microfabrication of capacitive ultrasonic transducers," *IEEE/ASME Microelectromech. Syst.,* vol. 7, p. 295–302, 1998.

[28] Jin X, Ladabaum I, Degertekin F L, Calmes S and Khuri-Yakub B T, " Fabrication and characterization of surface micromachined capacitive ultrasonic immersion transducers," *IEEE/ASME J. Microelectromech. Syst.,* vol. 8, pp. 100-114, 1999.

[29]   Eccardt P C, Niederer K, Scheiter T and Hierhold C, "Surface micromachined ultrasound transducers in CMOS technology," *Proc. IEEE Ultrason. Symp.,* pp. 959-62, 1996.

[30]   Eccardt P C, Niederer K and Fischer B, "Micromachined transducers for ultrasound applications," *Proc. IEEE Ultrason. Symp.,* vol. 2, p. 1609–18, 1997.

[31]   Huang Y, Ergun A S, Haeggstr¨om E, Badi M H and Khuri-Yakub B T, "Fabricating capacitive micromachined ultrasonic transducers with wafer-bonding," *IEEE/ASME J. Microelectromech. Syst.,* vol. 12, pp. 128-37, 2003.

[32]   Huang, Y.; Ergun, A.S.; Haeggstrom, E.; Khuri-Yakub, B. T., "Fabrication of Capacitive Micromachined Ultrasonic Transducers (CMUTs) using wafer bonding technology for low frequency (10 kHz-150 kHz) sonar applications," *OCEANS '02 MTS/IEEE,* vol. 4, pp. 2322-2327, Oct. 2002.

[33]   Goksen G. Yaralioglu, A. Sanli Ergaun, Khuri-Yakub BT, "Finite-Element Analysis of Capacitive Micromachined Ultrasonic Transducers," *IEEE Transactions on Ultrasonics, Ferroelectrics and Frequency Control,* vol. 52, no. 12, pp. 2185-2198, 2005.

[34]   Oralkan O¨ , Jin X, Degertekin F L and Khuri-Yakub B T, "Simulation and experimental characterization of a 2-D capacitive micromachined ultrasonic transducer array elemet," *IEEE Transactions on Ultrasonics, Ferroelectrics and Frequency Control,* vol. 46, pp. 1337-40, 1999.

[35]   Jin Xuecheng, Omer Oralkan, Degertekin F L and Khuri-Yakub B T, "Characterization of one dimensional capacitive micromachined ultrasonic immersion transducer arrays," *IEEE Trans. Ultrason. Ferroelectr. Freq. Control,* vol. 48, pp. 750-60, 2001.

[36]   Omer Oralkan , Ergun A S, Cheng C H, Johnson J A, Karaman M, Lee T H and Khuri-Yakub B T, "Volumetric ultrasound imaging using 2D CMUT arrays," *IEEE Trans. Ultrason. Ferroelectr. Freq. Control,* vol. 50, no. 11, p. 1581–94, 2003.

[37]   David T. Yeh, Omer Oralkan, Wygant IO, Ergun AS, Wong JH, and Khuri-Yakub BT, "High-Resolution Imaging with High-Frequency 1-D Linear

CMUT Arrays," *IEEE International Ultrasonics Symposium,* vol. 1, pp. 665-668, 2005.

[38]   Srikant Vaithilingam, Iran O. Wygant, Kuo PS, Zhuang X, Oralkan Ö, Olcott PD, Khuri-Yakub BT, "Capacitive Micromachined Ultrasonic Transducers CMUTs for Photoacoustic Imaging," *Proc. Of SPIE , Photons plus ultrasound: Imaging and Sensing,* vol. 6086, 2006.

[39]   Igal Ladabaum, Xuecheng Jin, Hyongsok T. Soh, Abdullah Atalar, Butrus T. Khuri-Yakub, "Surface Micromachined Capacitive Ultrasonic Transducers," *IEEE transaction on ultrasonics, ferroelectrics and frequency control,* Vols. 45, No. 3, pp. 678-690, 1998.

[40]   Min-Hang Bao, Micro Mechanical Transducers: Pressure Sensors, Accelerometers and Gyroscopes, Elsevier Science (October 30, 2000), Chapter.4, pp. 148, 2000.

[41]   Goksen G. Yaralioglu, Arif Sanli Ergun, Baris Bayram, Edward Haeggstrom and Butrus T. Khuri-Yakub, "Calculation and Measurement of Electromechanical Coupling Coefficient of Capacitive Micromachined Ultrasonic Transducers," *IEEE Transactions on Ultrasonics, Ferroelectrics, and Frequency Control,* vol. 50 (4), pp. 449-456, 2003.

[42]   S. Pacheco, P. Zurcher, S. Young, D. Weston and W. Dansker, "RF MEMS Resonator for CMOS Back End-Of-Line Integration," *5th Topical Meeting on Silicon Monolithic Integrated Circuits in RF Systems,* pp. 203-206, 2004.

[43]   Chowdhury, S.; Ahmadi, M.; Miller, W.C., "Nonlinear effects in MEMS capacitive microphone design," *Proceedings on MEMS, NANO and Smart Systems,* pp. 297-302, 2003.

[44]   S. Timoshenko, S Woinowsky-Krieger, Theory of plates and shells, 2nd ed., McGraw-Hill Book Company, 2nd Edition, pp. 55, 1959.

[45]   T. R. Hsu, MEMS and Microsystems- Design, Manufacture, and Nanoscalle Engineering, 2nd ed. ed., John Wiley & Sons, Inc., 2008.

[46] Werner Soedel, Vibrations of Shells and Plates, New York: Marcel Dekker, Inc., Chapter. 5,8,11, 1981.

[47] Wei You, Edmond Cretu, Rober Rohling, "Analytical Modeling of CMUTs in Coupled Electro-Mechano-Acoustic Domains Using Plate Vibration Theory," *IEEE SENSORS,* vol. 11, no. 9, pp. 2159-68, 2011.

[48] Lawrence E. Kinsler, Austin R. Frey, Alan B. Coppens and James V. Sanders, Fundamentals of Acoustics, 3rd ed., John Wiley & Sons, pp. 178, 1982.

[49] T.A. Emadi, G. Thomas, D.A. Buchanan, S. Pistorius, "A MEMS Ultrasonic Transducer Imager Array with Beam Width, Acoustic Power, and Frequency Modulations," *IEEE International Conference on Imaging Systems and Techniques (IST),* pp. 431-435, July 2012.

[50] "COMSOL Multiphysics User Guide, Theory for the Pressure Acoustic, Version 4.3," 2012. [Online].

[51] M. Moser, "Engineering Acoustics- An introduction to noise control," Springer, 2004.

[52] J. David N. Cheeke, Fundamentals and applications of ultrasonic waves, CRC Press, Chapter. 3, 6, pp. 55, 103, 2002.

[53] "PolyMUMPs Design Handbook, MEMSCAP Inc., Revision 13.0, 2011.," [Online].

[54] Agilent Technologies, February 2014. [Online]. Available: http://cp.literature.agilent.com/litweb/pdf/5950-3000.pdf.

[55] E. Richard Booser, Handbook of Lubrication: Theory and Practice of Tribology, CRC Press, page. 292, Volume 2, Theory and Design, 1983.